

Models for Metal-Poor Stars with Enhanced Abundances of C, N, O, Ne, Na, Mg, Si, S, Ca, and Ti, in Turn, at Constant Helium and Iron Abundances

Don A. Vandenberg

Department of Physics & Astronomy, University of Victoria, P.O. Box 3055, Victoria, B.C., V8W 3P6, Canada

vandenbe@uvic.ca

Peter A. Bergbusch

Department of Physics, University of Regina, Regina, Saskatchewan, S4S 0A2, Canada

pbergbusch@accesscomm.ca

Aaron Dotter¹

Department of Physics & Astronomy, University of Victoria, P.O. Box 3055, Victoria, B.C., V8W 3P6, Canada

Aaron.Dotter@gmail.com

Jason W. Ferguson

Department of Physics, Wichita State University, Wichita KS 67260-0032, U.S.A.

Jason.Ferguson@wichita.edu

Georges Michaud

Département de Physique, Université de Montréal, Montréal, Quebec, H3C 3J7, Canada

michaudg@astro.umontreal.ca

Jacques Richer

Département de Physique, Université de Montréal, Montréal, Quebec, H3C 3J7, Canada

jacques.richer@umontreal.ca

Charles R. Proffitt

Space Telescope Science Institute, 3700 San Martin Drive, Baltimore, MD 21218, U.S.A.

proffitt@stsci.edu

ABSTRACT

Recent work has shown that most globular clusters have at least two chemically distinct components, as well as cluster-to-cluster differences in the mean [O/Fe], [Mg/Fe], and [Si/Fe] ratios at similar [Fe/H] values. In order to investigate the implications of variations in the abundances of these and other metals for H-R diagrams and predicted ages, grids of evolutionary sequences have been computed for scaled solar and enhanced α -element metal abundances, and for mixtures in which the assumed $[m/\text{Fe}]$ value for each of the metals C, N, O, Ne, Na, Mg, Si, S, Ca, and Ti has been increased, in turn, by 0.4 dex *at constant* [Fe/H]. These tracks, together with isochrones for ages from ≈ 6 to 14 Gyr, have been computed for $-3.0 \leq [\text{Fe}/\text{H}] \leq -0.6$, with helium abundances $Y = 0.25, 0.29, \text{ and } 0.33$ at each [Fe/H] value, using upgraded versions of the Victoria stellar structure program and the Regina interpolation code, respectively. Turnoff luminosity versus age relations from isochrones are found to depend almost entirely on the importance of the CNO-cycle, and thereby mainly on the abundance of oxygen. Since C, N, and O, as well as Ne and S, do not contribute significantly to the opacities at low temperatures and densities, variations in their abundances do not impact the predicted T_{eff} scale of red giants. The latter is a strong function of the abundances of only Mg and Si (and Fe, possibly to a lesser extent), because they are so abundant and because they are strong sources of opacity at low temperatures. For these reasons, Mg and Si also have important effects on the temperatures of MS stars. Due to their low abundances, Na, Ca, and Ti are of little consequence for stellar models. The effects of varying the adopted solar metals mix and the helium abundance at a fixed [Fe/H] are also briefly discussed.

Subject headings: diffusion — globular clusters: general — Hertzsprung-Russell diagram — stars: abundances — stars: evolution — stars: interiors — stars: Population II — Sun: abundances

¹Current Address: Space Telescope Science Institute, 3700 San Martin Drive, Baltimore, MD 21218, U.S.A.

1. Introduction

It is now a well-established result that the observed chemical abundance variations in globular cluster (GC) stars are due to both evolutionary processes within them and variations in the chemical makeup of the gas out of which they formed. There is no doubt that extra nonconvective mixing (not yet fully understood, but see Denissenkov 2012 for recent advances in our understanding) operates in cluster giants brighter than the red-giant-branch (RGB) bump (Denissenkov & Vandenberg 2003, and references therein), which causes the surface abundances of C, N, and (sometimes) O to vary with luminosity. However, CN variations and the O–Na anticorrelation that appears to be characteristic of nearly all GCs (Carretta et al. 2009) have also been found in dwarf, turnoff, and subgiant stars (e.g., Cannon et al. 1998; Gratton et al. 2001; Ramírez & Cohen 2002; Cohen & Meléndez 2005; D’Orazi et al. 2010), where extra mixing is not a viable explanation. (NGC 5466 appears to be a notable exception to this insofar as little or no evidence has been found in this system for primordial star-to-star variations in the abundances of the light elements; see Shetrone et al. 2010.) Indeed, below the RGB bump, the chemical composition anomalies do not appear to vary with luminosity (also see Grundahl et al. 2002).

Further evidence for primordial abundance variations in GCs is provided by the detection of Mg–Al anticorrelations (see Yong et al. 2005). The stars currently on the main sequence (MS) and the RGB of these systems can hardly be responsible for the Al-rich, Mg-depleted (and, in a subset of the latter, Si-enhanced) stars that have been found in the most massive and/or the most metal-deficient clusters (like NGC 2808, NGC 6388, and M 15 — see Carretta et al. 2009) because their interiors are not hot enough for the Mg–Al cycle (and, especially, any additional processing to Si) to occur. As discussed by Carretta et al., the most likely explanation for the origin of the observed Mg, Al, and Si abundances is hot-bottom burning in intermediate-mass asymptotic-giant-branch (AGB) stars. In fact, there are cluster-to-cluster differences in the mean abundances of these elements as well as star-to-star differences within a given GC. For instance, as reported by Carretta et al., NGC 2808, M 4, and M 5, which have similar [Fe/H] values to within ≈ 0.3 dex, have mean [Mg/Fe] ratios of 0.20, 0.41, and 0.55, with *rms* variations of 0.25, 0.07, and 0.03 dex, respectively, while their [Si/Fe] values are, in turn, 0.28, 0.30, and 0.52, with *rms* variations amounting to ≈ 0.05 dex in each cluster. Interestingly, the average [O/Fe] value in the Carretta et al. sample of 17 GCs ranges from -0.30 in NGC 6388 to $+0.46$ in NGC 7099, with *rms* variations from ~ 0.1 dex in several systems to as high as 0.36 dex (in NGC 2808).

These results raise at least two obvious questions. Is the net effect of the scatter in the [m/Fe] value for each metal m , within a given cluster, large enough to cause a detectable spread in the effective temperatures, and hence the colors, of stars along the principal se-

quences that define its color-magnitude diagram (CMD)? Are cluster-to-cluster differences in the abundances of individual metals big enough to affect the difference in color between the turnoff and the lower RGB, which is a sensitive measure of the relative ages of GCs having very similar $[\text{Fe}/\text{H}]$ values (VandenBerg, Bolte, & Stetson 1990) and often used for that purpose (e.g., Marín-Franch et al. 2009)? VandenBerg & Stetson (1991) showed early on that this relative age diagnostic is affected by differences in $[\text{O}/\text{Fe}]$, but it is not yet clear whether it is also impacted by variations in the abundances of other α -elements, such as Ne, Mg, and Si, which are the most abundant metals after the CNO group.

Although there have been a few studies of metal-poor stellar models that allow for C–N–O–Na anticorrelations (notably Salaris et al. 2006, Cassisi et al. 2008, Pietrinferni et al. 2009), with some speculative discussion of the expected effects of Mg–Al anticorrelations (see the paper by Salaris et al.), the consequences of varying each of the most abundant metals, in turn, have yet to be adequately investigated. To be sure, we already have a very good understanding of the role played by C, N, and O in the evolution of lower mass stars and on computed isochrones (e.g., Rood & Crocker 1985, VandenBerg 1985, 1992¹). The same can be said for the case when the abundances of all of the α -elements vary together (e.g., Salaris, Chieffi, & Straniero 1993, VandenBerg et al. 2000, Kim et al. 2002, Pietrinferni et al. 2006). However, relatively little has been done to date to examine the dependence of model T_{eff} s on the abundances of individual α -elements heavier than oxygen.

The most noteworthy of the few available studies that have carried out such work is that by Dotter et al. (2007, also see Lee et al. 2009, who discuss some of the implications of the Dotter et al. results for integrated colors, Lick indices, and synthetic spectra), but their analysis is complicated by the fact that their computations were carried out at a constant value of Z (the mass-fraction abundance of all elements heavier than helium). This has the consequence that, when the abundance of one metal is increased, the abundances of all of the others are reduced. The net effect on stellar models therefore depends on how the surface and interior opacities have changed as a result of varying all of the elemental abundances at the same time, by different amounts. Fortunately, the problem is not as intractable as these

¹Dotter et al. (2007) incorrectly asserted that the models reported by VandenBerg (1992) “did not account for enhanced oxygen in the opacities”. In fact, opacity tables for temperatures > 1 eV ($\approx 12,000$ K) were derived for the assumed heavy-element abundances from the Los Alamos Astrophysical Opacity Library (Huebner et al. 1977), from which Rosseland mean opacities could be calculated for any mixture of the 20 most abundant elements. It was only the opacities for lower temperatures that were not obtainable at that time, but as mentioned therein and confirmed in the present investigation, oxygen does not contribute significantly to the low- T opacities because it has a high ionization potential and thus is a poor electron donor at the temperatures and densities characteristic of the outer layers of stars (also see Bell & Oke 1986, VandenBerg & Bell 2001).

few remarks suggest, because the $[\text{Fe}/\text{H}]$ values that are obtained for the cases when the abundances of most of the metals (except oxygen) are enhanced, in turn, differ by $\lesssim 0.05$ dex from that of the base mixture. Hence, the effects of varying the chemical composition at a constant Z is quite a good approximation to those derived when a single metal is enhanced at a constant value of $[\text{Fe}/\text{H}]$. Accordingly, the authors are able to confidently predict, for instance, that increased abundances of Mg and Si will result in cooler tracks and isochrones.

Still, since observers use number abundance ratios to describe the chemical compositions of stars, stellar models that vary the abundances of a single element at a constant $[\text{Fe}/\text{H}]$ value are much more straightforward to interpret. The latter approach, which is taken in the present study, has the advantage that the effects of altering the abundances of individual metals with can be accurately and precisely quantified. Moreover, whereas Dotter et al. (2007) considered only one (high) value of Z , we have generated large grids of tracks and isochrones for $[\text{Fe}/\text{H}]$ values ranging from -3.0 to -0.6 , in steps of 0.2 dex, on the assumption of $Y = 0.25, 0.29, \text{ and } 0.33$ at each adopted iron abundance. At the lowest metallicities, one can anticipate that variations in the abundances of elements heavier than oxygen will have little or no impact on stellar evolutionary computations, as the interior opacity at low Z is due primarily to bound-free and free-free processes involving H and He. The CNO elements, which are also considered here, differ from the heavier metals in that they affect the nucleosynthesis of hydrogen to helium, and thereby the structures of stars: an increase in the importance of the CNO-cycle due to enhanced abundances of these elements will make H-burning more centrally concentrated because of the high temperature sensitivity of these reactions compared to the *pp*-chain, and it is well known that the rate at which the radius of a low-mass star grows with time after leaving the zero-age main sequence (ZAMS) depends upon the rate at which its central concentration increases. These effects can be expected to be important at any metallicity.

2. The Heavy-Element Mixtures for Which Stellar Models have been Computed

Table 1 lists all of the heavy elements that are considered when requesting opacities for stellar interior conditions using the Livermore Laboratory OPAL opacity website², along with three different determinations of their abundances in the Sun. The most recent of these is by Asplund et al. (2009, hereafter A09), which updated the findings that were published by Asplund, Grevesse, & Sauval (2005, hereafter AGS5). As shown in Table 1, the CNO abun-

²<http://opalopacity.llnl.gov>

dances that were derived in these two studies differ by ≤ 0.05 dex, while the differences are generally in the range 0.05–0.10 dex for the heavier metals. Interestingly, neither of these results has found favor in the asteroseismology community (see, e.g., Pinsonneault & Delahaye 2009, Serenelli et al. 2009). While the inclusion of additional physics not normally considered in Standard Solar Models (SSMs) may help to reduce the discrepancies between the predicted and measured oscillation frequencies and improve the fit to the radial variation of the sound speed, when “Asplund” solar abundances are assumed in the models (e.g., Christensen-Dalsgaard et al. 2011, Bi et al. 2011), SSMs that adopt the solar abundances given by Grevesse & Sauval (1998, hereafter GS98) are still the least problematic ones.

In view of this ongoing controversy, we have chosen to generate grids of evolutionary tracks for the GS98 and the AGS5 cases, since it is of some interest to examine the impact that the adopted solar mix of metals has on isochrones for low values of $[\text{Fe}/\text{H}]$. As noted above, the differences between the solar $\log N$ values determined by AGS5 and A09 are quite small; consequently, the main results of this study will be essentially independent of this choice. Nevertheless, grids of models for the A09 abundances will be provided in a forthcoming paper.

Since the focus of this work is on metal-poor stars, an α -enhanced mix of heavy elements should be assumed in the reference models against which the computations for single-element enhancements are compared. Rather than simply adopting a constant 0.3 or 0.4 dex increase in the abundance of each α -element, the mean $[m/\text{Fe}]$ values that were determined by Cayrel et al. (2004) in their “First Stars” ESO Large Programme have been adopted: they are listed in the fifth column of Table 1. (Although these results strictly apply to stars with $[\text{Fe}/\text{H}]$ values $\lesssim -2.0$, very similar results have, for the most part, been found at higher metallicities — see, e.g., Yong et al. 2005.) Note that the Cayrel et al. determinations of $[m/\text{Fe}]$ for Cr and Mn have also been assumed, though this choice will not affect the computed stellar models because the abundances of these elements are so low in the metallicity regime under consideration. Be that as it may, additional grids of tracks were computed in which the GS98 and AGS5 $\log N$ abundances were adjusted by the $\Delta \log N$ values given in the fifth column of Table 1 and then scaled to the desired $[\text{Fe}/\text{H}]$ values. These sets of models were given the names GSCX and AGSC, respectively, where the “C” indicates “Cayrel” et al. $[m/\text{Fe}]$ abundance ratios. (Note that the GSCX models are the same ones that were used in the analyses of $BV(RI)_C JK_S$ photometry of field and GC stars by VandenBerg, Casagrande, & Stetson 2010 and Brasseur et al. 2010.)

Finally, additional model grids were computed for the same ranges of $[\text{Fe}/\text{H}]$ and Y noted above in which the abundance of C, N, O, Ne, Na, Mg, Si, S, Ca, and Ti was increased, in turn, by 0.4 dex over the AGSC abundances. The names that were assigned to these

computations are listed in the last column of Table 1. To distinguish the grids for different helium and iron abundances, we have adopted file names of the form “nnnnyijmkl”, where “nnnn” is the 4-letter designation for the assumed mixture (e.g., GS98, AGSC, AGxO), “yij” specifies the adopted helium abundance (e.g., “y25” represents $Y = 0.25$; the other choices are “y29” and “y33”), and “mkl” indicates the assumed $[\text{Fe}/\text{H}]$ value such that, for instance, “m30” and “m06” refer to $[\text{Fe}/\text{H}] = -3.0$ and -0.6 , respectively. Argon is the only α -element that was not subjected to the same analysis as the others: its effects on tracks and isochrones should be similar to those for neon, but at a much reduced level, given that it has a lower abundance by ~ 1.6 dex. Aside from C and N, the only element not a member of the α -group for which stellar models were generated with and without an enhanced abundance is Na.

3. The Victoria Stellar Evolution Code

A number of important improvements have been made to the Victoria stellar structure and evolution code since it was last used for extensive grid computations (VandenBerg, Bergbusch, & Dolez 2006). The most significant one is the inclusion of the diffusion of hydrogen, helium, and the light elements ${}^6\text{Li}$, ${}^7\text{Li}$, and ${}^9\text{Be}$ (but not the heavier metals) using the numerical methods that are described in considerable detail by Proffitt & Michaud (1991, see the Appendices of this paper), along with the revised treatment of thermal diffusion reported by Proffitt & VandenBerg (1991). [The LiBeB elements are treated only to constrain the extra mixing that is needed to limit the efficiency of gravitational settling from the surface layers of stars — see below. Spectroscopic studies have found either no detectable difference in the surface abundances of Population II stars between the turnoff and the lower RGB (e.g., Gratton et al. 2001, Ramírez & Cohen 2002) or a small variation, amounting to $\lesssim 0.15$ dex, which can be made consistent with the predictions of stellar models if some additional (turbulent) mixing just below surface convection zones is taken into account (Korn et al. 2006). The models computed for the Korn et al. study also included radiative accelerations: as emphasized by Richard et al. (2002), “it is a better approximation not to let Fe diffuse at all in a $0.8\mathcal{M}_\odot$ star than to calculate its gravitational settling without including the effects of $g_{\text{rad}}(\text{Fe})$ ”. Radiative accelerations have also been found to have interesting ramifications for the chemical abundance profiles in the vicinity of the H-burning shell in low-mass red giants (see Michaud et al. 2010).]

Worth mentioning is the fact that the chemical abundance changes due to nuclear burning, convective mixing, turbulent transport, and ionic diffusion are considered simultaneously. Indeed, because of the transport terms, it is necessary to solve the relevant equa-

tions for all of the species in all zones at the same time, using a layer-by-layer Newton-Raphson scheme similar to that employed to solve the stellar structure equations (e.g., Henyey, Forbes, & Gould 1964). (Any surface and central convective regions that exist are treated as if they were single, uniformly mixed zones, with mass-averaged initial abundances and nuclear reaction rates.) Since the solution to the chemical composition equations affects the solution of the stellar structure equations, and vice versa, it is necessary to alternately solve both sets of equations in order to obtain a mutually consistent solution for a given timestep. Care is taken to ensure that the diffusion terms transport, but not create or destroy, the total amount of each species, and moreover, that the creation and destruction of the various isotopes by the nuclear terms balance appropriately. Diffusion coefficients are calculated using the spline fits to the collision integrals for a screened Coulomb potential given by Paquette et al. (1986).

We opted to retain the practice of solving the four stellar structure equations only in the innermost 99% of the total mass of the model star, and deriving the boundary conditions at that point through Runge-Kutta integrations of three of these equations, assuming that the integrated luminosity is constant in the surface layers (for a detailed description see VandenBerg et al. 2008; section 2.2). With this approach, it is possible to follow the large radial variations in the thermodynamic quantities in the outer 1% of the mass, as well as changes in the size of the convective envelope (especially when it contains $\ll 1\%$ of the star’s mass), very accurately by using small integration steps. It is well known that gravitational settling causes the surface abundances to change the most rapidly when the convective envelope is the thinnest (see, e.g., Proffitt & Michaud 1991). Surface convection zones having fractional masses $\Delta\mathcal{M}_{\text{SCZ}}/\mathcal{M}_* = 1 - \mathcal{M}_{\text{BCZ}}/\mathcal{M}_* > 2 \times 10^{-12}$, where $\Delta\mathcal{M}_{\text{SCZ}}$ is the mass of the surface convection zone, \mathcal{M}_{BCZ} is the mass interior to the base of the surface convection zone, and \mathcal{M}_* is the total stellar mass, are resolved by the Victoria code. If the convective-radiative boundary shrinks to the point where the fractional convective envelope mass falls below this value, the convective envelope is assumed to consist of a single shell having a fractional mass of 2×10^{-12} .

When the outer convection zone contains $< 1\%$ of the total stellar mass, an additional envelope integration (i.e., besides those needed to formulate the boundary conditions) must be performed at the end of each iteration of the Henyey solution scheme in order to determine the chemical abundance profiles in the entire radiative region of the stellar model. In practice, such integrations, for the $\log g$, T_{eff} , and surface abundance properties of the stellar model, are necessary only for the portions of the tracks for $\sim 0.8\mathcal{M}_{\odot}$, metal-poor stars from somewhat below the turnoff until approximately the middle of the subgiant branch. During the subsequent evolution, the convective envelope deepens rapidly and the radiative-convective boundary moves into the “interior” part of the stellar model (where all four stellar

structure equations are solved). Thus, our procedure is computationally more efficient than the alternative of solving for the entire structure from $\mathcal{M} = 0$ to $\mathcal{M} = \mathcal{M}_*$ using, e.g., the Henyey technique. In practice, slightly deeper envelope integrations are performed so that one can deal with the case in which the fractional mass in the convective envelope changes from just over 1% to just under 1% in a single timestep.

As already mentioned, uninhibited diffusion in the surface layers of Pop. II stars is ruled out by spectroscopic observations of turnoff and lower-RGB stars in GCs. Indeed, the hot end of the Li abundance “Spite plateau” (Spite & Spite 1982) cannot be reproduced by diffusive models *unless* extra mixing below envelope convection zones is taken into account (Richard et al. 2002). On the assumption that turbulence is the most important process that competes with atomic diffusion, Richer, Michaud, & Turcotte (2000, also see Richard, Michaud, & Richer 2001) devised a simple expression for the turbulent diffusion coefficient in terms of the atomic diffusion coefficient of helium at a density $\rho_0 = \rho(T_0)$ multiplied by $c(\rho_0/\rho)^n$, where the constant c , the exponent n , and the reference temperature T_0 are chosen so as to obtain the best match of the predicted and observed abundances.

Although we could have treated turbulent mixing in the same way, we discovered, as the result of a limited exploration of other ways of defining the turbulent diffusion coefficient, that the expression

$$D_{\text{turb}} = c(\rho_{\text{BCZ}}/\rho)^3/(1 - \mathcal{M}_{\text{BCZ}}/\mathcal{M}_*)^n ,$$

where c is a constant, ρ_{BCZ} is the density at the base of the surface convection zone, and ρ is the local density, worked at least as well as the expression given by Richer et al. (2000). (Due to the steep power-law dependence of the density ratio, $D_{\text{turb}} \ll 1$ in the nuclear-burning regions of the stellar model, which ensures that the assumed turbulence will not affect the chemical profiles resulting from nucleosynthesis and gravitational settling.) For instance, when we adopt 15.0 for the constant and $n = 1.5$, a Standard Solar Model for the GS98 metals mix is predicted to have a surface Li abundance of $\log N = 1.10$ (the observed value; see the tables provided by GS98), when 3.31 is the assumed initial value. (This constraint can be satisfied just as well by an SSM for the AGS5 solar abundances if c is set to a value of 33.0.) Furthermore, using exactly the same equation, with the values of the free parameters from the solar calibration, in the computation of an evolutionary track for a $0.76\mathcal{M}_\odot$ model having $Y = 0.25$, and $[\text{Fe}/\text{H}] = -2.4$, which has a predicted age of 13.5 Gyr at the turnoff, we obtain surface Li abundances that vary from the assumed initial value of $\log N = 2.58$ (Cyburt, Fields, & Olive 2003) to 2.10, which agrees rather well with the measured Li abundances in the “Spite plateau” stars. However, we note that the primordial Li abundance from the concordance of WMAP and Big Bang nucleosynthesis (BBN) has recently been revised upwards from 2.58 to 2.72 (Cyburt, Fields, & Olive 2008); consequently, a discrepancy ~ 0.15 dex remains. Encouragingly, evolutionary calculations

that were carried out for several different $[\text{Fe}/\text{H}]$ values (between -3.0 and -1.8), and a small range in mass (consistent with turnoff ages from 10 to 14 Gyr), yielded quite similar Li abundances values along the upper MS and turnoff.

In view of these results, the simple expression given above for the turbulent diffusion coefficient was adopted in all of the evolutionary computations that are presented in this study. We hasten to add, however, that it has been subjected only to the aforementioned tests so far and it could lead to problems when examined more thoroughly. This is left for future work to determine. For the time being, we can be reasonably confident that this choice does not adversely affect the T_{eff} scale of our models, which is perhaps the main concern with respect to the present paper, because VandenBerg et al. (2010) have already shown that the predicted temperatures along isochrones for the GSCX abundances agree very well with those derived by Casagrande et al. (2010) for a large sample of field stars that have M_V values based on *Hipparcos* parallaxes and which span a wide range in $[\text{Fe}/\text{H}]$. Although our treatment of extra mixing below envelope convection zones is very *ad hoc*, our results nevertheless suggest that stellar interior processes (yet to be understood) will eventually be found to be responsible for the difference between the observed Li abundances that define the “Spite plateau” and the primordial abundance from WMAP-BBN.

Besides the incorporation of diffusion and turbulent mixing, recent improvements to the rates of several nuclear reactions are now included in the Victoria code. In particular, the rates given by Junker et al. (1998) for ${}^3\text{He}({}^3\text{He}, 2p){}^4\text{He}$, by Confortola et al. (2007) for ${}^3\text{He}({}^4\text{He}, \gamma){}^7\text{Be}$, and by Junghans et al. (2003) for ${}^7\text{Be}(p, \gamma){}^8\text{Be}$ have been adopted, along with the rate of the important “bottle-neck” ${}^{14}\text{N}(p, \gamma){}^{15}\text{O}$ reaction by Marta et al. (2008). As far as He-burning reactions are concerned, we have opted to use the rates for the triple- α and the ${}^{12}\text{C}(\alpha, \gamma){}^{16}\text{O}$ reactions reported by Fynbo et al. (2005) and Hammer et al. (2005), respectively. For all nuclear reactions not explicitly mentioned, rates have been taken from the NACRE compilation (Angulo et al. 1999). Whereas OPAL opacities are used for temperatures $\gtrsim 10^4$ K, as already noted in § 2, complementary low-T opacities for all of the assumed chemical abundance mixtures have been generated using the computer code described by Ferguson et al. (2005). In addition, we have implemented the conductive opacities presented by Cassisi et al. (2007). Although some time was spent to install the sophisticated equation-of-state (FreeEOS) developed by A. Irwin³, which is undoubtedly superior to our default EOS (see the Appendix in VandenBerg et al. 2000), we decided to continue using the latter for this project because it is much faster (by about a factor of 3) and, more importantly, the impact of this choice on predicted evolutionary tracks and lifetimes is barely noticeable.

³See <http://freeeos.sourceforge.net>

The main difference is, in fact, a reduction in the predicted age of a star at the RGB tip by $\lesssim 1\%$ when the FreeEOS is employed, which is commensurate with a very slight shift in luminosity along the track.

We conclude this section with two final points. First, the diffusion physics described above is taken into account only during the evolution from just prior to reaching the ZAMS until the end of the subgiant branch. For the remaining evolution to the RGB tip, the implementation described by VandenBerg (1992) of the non-Lagrangian method of solving the stellar structure equations that was developed by Eggleton (1971) is used. This enables one to compute RGB loci for low-mass red giants very efficiently (typically requiring $\lesssim 1$ *cpu*-minute per giant-branch track on a 3 GHz PC) without losing any accuracy insofar as such predictions as the luminosity of the RGB bump and the helium core mass at the onset of the helium flash are concerned (see the next section). The neglect of diffusive processes during the relatively short lifetimes of red giants appears to have only minor consequences, judging from the work of Michaud et al. (2010, also see Hu et al. 2010, who have introduced atomic diffusion with an approximate treatment of radiative accelerations into the Eggleton formalism).

The second point worth noting is that the pressure at $T = T_{\text{eff}}$ is determined by integrating the hydrostatic equation from very small optical depths to the photospheric value, in conjunction with a scaled T - τ relation (from VandenBerg & Poll 1989) that reproduces the empirical solar atmosphere of Holweger & Mueller (1974). As discussed by VandenBerg et al. (2008), boundary pressures which are derived in this way agree very well with those predicted by scaled, differentially-corrected MARCS model atmospheres over wide ranges in temperature, gravity, and metallicity. Moreover, the resultant T_{eff} scale is nearly identical with that derived by Casagrande et al. (2010) for field subdwarfs having $-2.0 \lesssim [\text{Fe}/\text{H}] \lesssim -0.6$ using the infra-red flux method (see VandenBerg et al. 2010). This provides empirical support for our adopted treatment of the surface boundary conditions, as does the finding that the present models are able to match the morphologies of globular cluster CMDs quite well, except (possibly) at the lowest metal abundances (see VandenBerg et al. 2010).

3.1. Comparisons of Stellar Models Computed Using Different Codes

Figure 1 compares evolutionary tracks that have been computed using the Victoria and the MESA (version 3168; Paxton et al. 2011) codes for $0.8M_{\odot}$ models having initial values of $Y = 0.25$ and $[\text{Fe}/\text{H}] = -2.0$ (assuming the GS98 metals mix). For this comparison, the same value of the mixing-length parameter, $\alpha_{\text{MLT}} = 2.0$, was assumed, and photospheric pressures were derived by integrating the hydrostatic equation on the assumption

of the Krishna Swamy (1966, see equation 33) T - τ relation. The tracks with the coolest turnoffs take diffusive processes into account, while those with the hottest turnoffs neglect this physics. Aside from MESA using the Thoul, Bahcall, & Loeb (1994) treatment of gravitational settling, both computer programs incorporate the same, or very similar, basic physics (opacities, nuclear reaction rates, thermodynamics, convection theory). Even so, it is remarkable that two completely independent codes predict nearly identical tracks from the ZAMS to the RGB tip with, or without, including the settling of helium. The most noticeable difference occurs near the turnoffs of the diffusive tracks, which can probably be attributed to the different treatments of diffusion in the two codes since there is no significant offset of the turnoff T_{eff} s in the tracks without diffusion. At the tip of the giant branch, the ages, luminosities, and helium core masses agree to within $\sim 2\%$, $\delta \log L/L_{\odot} = 0.015$, and 0.0007 solar masses, respectively. Such small variations can easily be attributed to the uncertainties in the input physics; e.g., they are reduced by about a factor of two if the equation of state normally used in the Victoria code is replaced by FreeEOS (see the previous section).

To illustrate the extent to which low-metallicity tracks are affected by metals diffusion, a track (the dotted curve) has been computed using the same version of the MESA code, except that the settling of the heavy-elements has also been treated (i.e., in addition to helium). As expected, the track evolves to warmer turnoff temperatures during the core H-burning phase due to the settling of the metals below the increasingly thin convective envelope. Because most of those metals are dredged back into the surface during the evolution along the subgiant branch when convection penetrates into the interior layers, the track subsequently merges with the one that allowed only for helium diffusion (the dashed curve). However, as already noted, uninhibited diffusion has been ruled out by spectroscopic observations, which have found little or no difference between the $[\text{Fe}/\text{H}]$ values for stars near the turnoff and those on the lower RGB. If extra mixing is invoked to minimize the variation of the metal abundances during the evolution between the ZAMS and the turnoff, the resultant track is shifted to somewhat lower effective temperatures (see the plots provided by Richard et al. 2002).

Given that surface abundance changes are a strong function of the size of the convective envelope, Figure 2 provides an especially compelling demonstration that the treatments of diffusion in both codes are very similar. The upper panel shows how the fraction of the total mass contained within the surface convection zone varies with age for the ZAMS to lower-RGB portions of the diffusive tracks in the previous figure. The lower panel plots the corresponding temporal variation of the surface mass-fraction abundance of helium, Y_{S} , for the same sequences. The agreement is clearly very good. Note that Y_{S} is predicted to decrease almost to zero when extra (turbulent) mixing below surface convection zones is ignored, which is the case in the diffusive tracks considered in Figs. 1 and 2.

Although stellar models for super-metal-rich stars are not considered here, we decided to compare Victoria and MESA tracks for such a case simply to show that the excellent agreement obtained at low metallicities is also found when very different masses and chemical abundances are assumed. Figure 3 is similar to Fig. 1, except that the evolutionary sequences which are plotted were generated for a $1.10M_{\odot}$ star, having initial helium and metal abundances corresponding to $Y = 0.30$ and $[\text{Fe}/\text{H}] = +0.30$ (assuming the GS98 $[m/\text{Fe}]$ ratios for all other metals). At most luminosities, the predicted T_{eff} s agree to within a few Kelvin, with the largest differences amounting to ~ 30 K near the MS turnoff. Moreover, at the RGB tip, the ages agree to within 1.3%, the luminosities to within $\delta \log L/L_{\odot} = 0.011$, and the helium core masses to within 0.0012 solar masses. This level of consistency is really very satisfactory.

We have also carried out some comparisons with respect to models produced by the Montreal code (see Michaud et al. 2004; and references therein). However, such comparisons are less straightforward to carry out given that, in particular, the latter use monochromatic opacities to calculate the Rosseland opacities at each layer in a stellar model and at each evolutionary timestep (also see Turcotte et al. 1998). As noted by Michaud et al., opacity data that are derived in this way, rather than from interpolations in pre-computed OPAL tables for a fixed metals mixture (which is the approach used in the Victoria and MESA codes), have consequences for the solar-calibrated value of α_{MLT} because the variations in the relative abundances of C, N, and O arising from the operation of the CNO-cycle will modify the opacity profile in stellar interiors. Encouragingly, if the value of α_{MLT} is suitably chosen so that ZAMS models for a given mass and chemical composition have the same convective envelope mass when generated by either the Victoria or Montreal codes, the predicted variations of $\Delta M_{\text{SCZ}}/M_{*}$ and Y_{S} with time are nearly the same. (Plots to illustrate this are not included here because the level of agreement is comparable to that shown in Fig. 2.) This indicates that the treatments of diffusive processes which are employed by the Victoria and Montreal (and MESA) codes lead to very similar effects. In fact, isochrones for very metal-poor stars that are obtained from grids of evolutionary tracks computed using the Montreal code can also be reproduced rather well by current Victoria computations — even though the former, but not the latter, take the diffusion of the metals and radiative accelerations into account.

4. Framework for Interpolations in the Model Grids

The ultimate goal of the interpolation methods that we have employed over the years (Bergbusch & Vandenberg 1992; Bergbusch & Vandenberg 2001; Vandenberg, Bergbusch, & Dowler

2006) is to produce isochrones, luminosity functions, and isochrone population functions that represent the underlying canonical models as accurately as possible. With this new set of model grids, we add the ability to interpolate grids of tracks with arbitrary helium abundances and/or metallicities encompassed by the canonical grids.

The original isochrone interpolation scheme (Bergbusch & Vandenberg 1992) relied on the identification of seven primary equivalent evolutionary phases (EEPs): 1) the zero-age main sequence (ZAMS), 2) the main-sequence turn-off (MSTO), 3) the blue hook (BLHK), 4) the Hertzsprung gap (HZGP), 5) the base of the red-giant branch (BRGB), 6) the giant-branch pause (GBPS), and 7) the giant-branch tip (GBTP) on the tracks. (However, as will be explained below, we have dispensed with the HZGP EEP; consequently, interpolations in the current models rely on only six primary EEPs.) This particular set of EEPs was chosen because they trace the mathematical properties of the tracks; some of them also mark significant evolutionary events. Except for the ZAMS and GBTP EEPs, they can be recognized exclusively by the morphology of the temporal derivative of the effective temperature (i.e., $d(\log T_{\text{eff}})/d(\log t)$) and all of them can be detected automatically. Most importantly, except for some situations in the metal-rich grids when the CNO cycle begins to emerge as the dominant source of energy production in the higher mass tracks and blue hook morphology starts to develop, the age–mass relation for each of the primary EEPs is monotonic and all of the interpolation relations (e.g., age–mass, luminosity–mass, or temperature–mass) are very nearly linear. As illustrated in Figure 1 of Bergbusch & Vandenberg (2001), it is easy to recover monotonic behaviour in the age–mass relations by minor adjustments to the location of the MSTO and/or BLHK EEPs on the tracks that fall in this transition region.

When the effects of helium diffusion are included in the model calculations, a bump feature manifests itself in the subgiant branch region with an intensity and an extent that is affected by the assumed chemical abundances. Problematically, this bump feature migrates across the HZGP EEP as a function of track mass (though it occurs at a nearly constant value of T_{eff}). Furthermore, the HZGP EEP as we originally defined it is an artifact of pp -chain processing and it becomes less significant in tracks of higher mass. Since it is difficult to detect the HZGP automatically in tracks that include helium diffusion and in tracks where the CNO cycle dominates the energy production, we elected to dispense with it and hence to construct the interpolation scheme around the remaining six primary EEPs.

The identification of the ZAMS EEP presents an interesting challenge because the pre-main-sequence (PMS) contraction phases of evolution produce quite different morphologies depending on the mass of the track and the chemical composition of the grid. After considering other possibilities, we decided to adopt a ZAMS criterion based on the initial hydrogen content that also takes into account the iron abundance of the grid as well as the mass of

the track itself:

$$X_{\text{ZAMS}} = X_{\text{init}} - 0.0007 - (3.0 + [\text{Fe}/\text{H}]) \times (1.667 \times 10^{-4} + 4.167 \times 10^{-4}(\mathcal{M}/\mathcal{M}_{\odot} - 0.4)).$$

This formulation, which steps past the complicated morphology in the late contraction phases of the higher mass stellar models, produces monotonic, smoothly varying age-mass relations connecting the ZAMS EEPs. (For masses considered in this investigation, the differences between the resultant ZAMS models and those based on an $L_{\text{grav}}/L < 1\%$ prescription are quite minor. Over the entire range in $[\text{Fe}/\text{H}]$ and Y for which evolutionary tracks have been computed for the different choices of the chemical abundances, the two criteria yield values of $\log L$ and $\log T_{\text{eff}}$ that differ by 0.0–0.015 and 0.0–0.0010, respectively, nearly independently of the assumed mass, while age differences range from 0.0–0.017 Gyr, in the case of $1.2\mathcal{M}_{\odot}$ models, to ~ 0.06 Gyr, in the case of $0.4\mathcal{M}_{\odot}$ models.)

It is, in fact, fundamental to the interpolation scheme that age be a monotonic function of mass for a given primary EEP. In previous papers, we divided the regions between the primary EEPs into equidistant secondary EEP intervals via the metric

$$\Delta\mathcal{D} = [1.25(\Delta \log L)^2 + 10.0(\Delta \log T_{\text{eff}})^2]^{1/2}$$

under the assumption that stellar evolution proceeds in a uniform way. (The right-hand side of the above equation is an arbitrary definition of the “distance” along a track.) It turns out that this assumption is not strictly valid over the range of chemical abundances and track masses encompassed by the new grids, particularly on tracks for models in which CNO energy production becomes competitive with pp -chain energy production between the ZAMS and the MSTO EEP. In the new grids, we employed the distance metric

$$\Delta\mathcal{D} = [4.0[(\Delta \log t)^2 + 1.25(\Delta \log L)^2 + 10.0(\Delta \log T_{\text{eff}})^2]^{1/2}$$

to distribute the secondary EEPs in a way that maintains the monotonicity of the age–mass relations.

4.1. Preparation of the Canonical Grids

To ensure that all astrophysically significant regions of the HR-diagram would be mapped by the interpolation scheme, we evolved each track to an age of 30 Gyr (at least) or to the RGB tip, whichever came first. A maximum evolutionary age of 30 Gyr ensures that the isochrones that are interpolated within the canonical grids do not have any gaps in the point distribution. However, since evolution proceeds at a faster rate when, for example, the helium abundance is increased, and since we chose to use 3-point interpolations between the

grids of tracks, we actually had to increase the maximum evolutionary age for some tracks in the lower- Y grids to ensure that the tracks interpolated between the canonical grids would be complete.

Each canonical grid was processed (via the Akima spline, see Bergbusch & Vandenberg 2001) into a set of tracks consisting of secondary EEPs equidistantly spaced between successive primary EEPs. The corresponding regions of each track contain exactly the same number of secondary EEPs. For tracks that do not evolve as far as the MSTO, we used the central hydrogen content to match up the secondary EEPs. The result of all of this is that each canonical grid contains tracks that have matching complementary secondary EEP distributions across the range of masses encompassed by them. For example, the 235th secondary EEP in *any* track that has at least that many points is matched to the same point in every other track in every other grid. Grids of tracks at intermediate abundance parameters are constructed track by track simply by interpolating between matching secondary EEPs in the canonical grids with abundance parameters that encompass the interpolants. For each abundance mixture in this study, canonical grids were computed for thirteen $[\text{Fe}/\text{H}]$ values and for three different Y values at each iron abundance. Three-point interpolation in both $[\text{Fe}/\text{H}]$ and Y is used to produce grids at intermediate abundances.

4.2. Interpolation tests

The most obvious test of our interpolation methods is to compare a grid of tracks that has been interpolated from the canonical grids to a grid with the same abundance parameters computed directly using the Victoria code. The most challenging interpolations occur in grids of high metallicity and high helium abundance because these are the ones in which blue hook morphology manifests itself most strongly in the intermediate-mass stars. As illustrated by the examples shown in Figure 4, the interpolated tracks match the computed tracks extremely well — the only differences which are visible, at the scale of the plot, appear along the blue hook of the $1.1M_{\odot}$ track in the left-hand panel. In Figure 5, we superimpose isochrones for the ages 4, 5, 6, 7, 8, 10, 12, and 14 Gyr that have been interpolated from the interpolated tracks over those interpolated directly from the test set of tracks. Again, at the scale plotted, the only noticeable differences are seen along the nascent blue hook portions of the two youngest isochrones in the left-hand panel. The most critical tests of the interpolation scheme are shown in Figure 6, where we plot the differential isochrone population functions (DIPFs; see Bergbusch & Vandenberg 2001). Again, there are virtually no detectable differences at the plotted scale.

5. The Effects of Chemical Abundance Variations on Stellar Evolutionary Tracks and Isochrones

In order to carry out the most thorough examination of the impact of varying the mix of heavy elements on evolutionary tracks and isochrones, one should use fully consistent model atmospheres to derive both the surface boundary conditions for the stellar interior models and the color– T_{eff} relations that are needed to transpose the latter to the various CMDs of interest (e.g., Cassisi et al. 2004, Sbordone et al. 2011). Unfortunately, no such atmospheric models are currently available. However, varying the abundance of a single metal should not affect the temperature structure of the atmosphere (i.e., the T – τ relation) very much (particularly for upper-MS to lower-RGB stars), and it is well known that colors are much more dependent on temperature than on metallicity. Thus, while our results should describe *most* of the effects of chemical abundance variations on the predicted T_{eff} scale, and thereby on the model colors, there will be some second-order effects that cannot be determined until fully consistent “atmosphere-interior” models are computed for the assumed abundance mixtures.

The following analyses will mainly consider stellar models for $[\text{Fe}/\text{H}] = -1.0$ and -2.0 , given that the majority of the Galactic GCs have metallicities between these values. Note that, for most of the metals which are considered, an increase in the assumed $[m/\text{Fe}]$ value by 0.4 dex is appreciably larger than the observed variations within a given GC or from cluster-to-cluster at a given $[\text{Fe}/\text{H}]$. As a result, the predicted effects of such enhancements on H-R diagrams should be appropriately adjusted to reflect the actual chemical abundance variations under consideration. While it seems reasonable to expect that the net effect of increasing the abundances of two metals at the same time is equivalent to the sum of the effects of enhancing each metal separately, especially at low metallicities, it is not known whether this is necessarily the case. This and other issues will be addressed in a follow-up study.

5.1. Increasing the Abundances of Several Metals, in Turn

5.1.1. Consequences for Stellar Evolutionary Tracks

We begin our analysis by comparing the opacities for the different heavy-element mixtures at the same densities, temperatures, and hydrogen mass-fraction abundances, where the latter have been taken from the computed structures of representative stellar models. The left-hand panels of Figure 7 plot, as a function of $\log T$, the ratio of the opacity for each of the “enhanced” mixtures (e.g., AGxC, AGxN, etc., see Table 1) to that for the reference

mixture (AGSC). These opacities were calculated for the variations of ρ and X_{H} with T that describe the structure, from the outermost layers to the center, of a somewhat evolved $0.9M_{\odot}$ model in the AGSC grid having $Y = 0.25$ and $[\text{Fe}/\text{H}] = -1.0$. The “outermost layers” include that part of a stellar model which is determined by integrating $dP/d\tau = g/\kappa$ from very small optical depths to the value of τ where $T = T_{\text{eff}}$ in order to extend the evaluation of the opacity ratio to the lowest temperatures that are normally considered in a stellar model. The upper-left panel shows, for instance, that C, N, and O are important sources of opacity at temperatures above $\log T \sim 5.5$, while they do not contribute significantly to the opacity at low temperatures. The differences in the maximum value of the opacity ratio, which vary from ≈ 1.05 in the case of nitrogen to ≈ 1.50 in the case of oxygen, primarily reflect the differences in the abundances of these elements. From the additional panels along the left-hand side, one sees that (i) Mg and Si are important contributors to the opacity at both low and high temperatures, (ii) Ne and S are significant opacity sources only at relatively high temperatures, and (iii) the contribution of Na and Ti to the opacity is negligible (due mainly to their low abundances). Interestingly, despite their low abundances, Na and Ca affect the low- T opacities more than most of the other metals, although the differences are barely discernible at the plotted scale (at least at $[\text{Fe}/\text{H}] = -1.0$).

Significant changes to the opacity will affect the structure of a stellar model and, in turn, the location of its track on the H-R diagram. In particular, higher interior opacities will tend to shift an evolutionary sequence to lower luminosities and effective temperatures, whereas the predicted T_{eff} , but not the luminosity, is dependent on the low- T opacities. The right-hand panels of Fig. 7 plot the tracks for the reference AGSC mixture along with the tracks in which each of the 10 metals from C to Ti is given an enhanced abundance, in turn, by 0.4 dex. As Y and the $\log N$ abundances of all of the other metals are kept the same, the adopted enhancement will increase Z slightly, and therefore, the value of X that is assumed in the computed tracks must be decreased in order that $X + Y + Z = 1.0$. (Note that the line-type identifications are the same as in the left-hand panels.)

Because oxygen is the most abundant of all of the heavy elements and because it, like C and N, alters stellar models through both opacity and nucleosynthesis effects, it has the biggest impact, followed by Si, Mg, Ne, S, and C (in the order of decreasing influence), with the other metals having little or no effects. Because the CNO group, as well as Ne and S, are poor electron donors at low temperatures, the location of the lower RGB is unaffected by variations in the abundances of these elements. However, the giant-branch is shifted to significantly cooler temperatures (by ~ 100 K in lower mass stars having $[\text{Fe}/\text{H}] \approx -1.0$) if the abundance of Mg or Si is increased by 0.4 dex over their abundances in the reference mixture (which already has $[\alpha/\text{Fe}] = 0.4$). *(It is important to remember that the effects that any element has on evolutionary tracks and isochrones depend on the total amount of*

that element which is present. The above results apply only to the particular case under consideration; *i.e.*, the consequences of the same increase in the $[m/Fe]$ value of any metal would be smaller if the reference model assumed $[\alpha/Fe] = 0.0$, or if a lower $[Fe/H]$ value were considered.)

The filled and open circles on the reference AGSC track indicate the locations of the models from which the runs of ρ and X_H as a function of T were taken in order to generate the opacity data that are plotted in the left-hand panels of Fig. 7 and in Fig. 8, respectively. The two sets of plots look nearly identical, except at low temperatures, where the opacity ratios reach higher values in the case of the lower-RGB model because its atmospheric layers are cooler than in the MS model. The differences are especially large when the abundances of Mg or Si are enhanced, though the increased contributions of C and Ca to the low-temperature opacities are also apparent (albeit still very small). As shown below in our discussion of upper-RGB stars, their effects on predicted H-R diagrams are more conspicuous in stars of lower T_{eff} .

Although we do not have opacity data for heavy-element mixtures in which only the abundance of Fe is increased, it is possible to make an estimate of the relative importance of this element for opacities and evolutionary sequences if it is assumed that the effects due to individual elements are additive. The dotted curves in Figure 9 reproduce all of the loci that were originally plotted in Fig. 7, while the solid curves are obtained when *all* of the metals are simultaneously given increased abundances by 0.4 dex. Put in a different way, the thick and thin solid curves in the right-hand panel represent $0.9M_{\odot}$ tracks for $[Fe/H] = -1.0$ and -0.6 , respectively, when both assume the AGSC metals mixture. Relative to the lower metallicity case, the models for $[Fe/H] = -0.6$ obviously have higher abundances of all of the metals by $\delta \log N = 0.4$. If the differences in $\log T_{\text{eff}}$ and M_{bol} between the thick solid curve and each of the dotted curves, as measured along common EEP points, are summed, and then added to the track for $[Fe/H] = -1.0$, the result is the dashed curve. It seems reasonable to attribute the (surprisingly small) offset between this locus and the thin solid curve to the additional opacity sources that have not yet been taken into account; namely, Al, P, Cl, Ar, K, Cr, Mn, Fe, and Ni (see Table 1). Of these, iron is the most abundant element, by far; consequently, the differences between these curves is presumably due mostly to Fe.

The fraction of the total opacity, and its distribution with temperature, that is contributed primarily by iron is expected to be approximately the difference between the solid and the dashed curves in the left-hand panel of Fig. 9. The solid curve plots, as a function of $\log T$, the ratio of the opacity for $[Fe/H] = -1.0$ to that for $[Fe/H] = -0.6$, assuming the reference AGSC metals mixture in both cases. As in previous plots, the opacities were

computed for the values of T , ρ , and X_{H} that give the surface-to-center variations of these quantities in the MS model which has been plotted as a filled circle in the right-hand panel. The dashed curve, on the other hand, shows how $1 + \Sigma[\delta(\text{opacity ratio})]$ varies with temperature, where the second term denotes the sum of the dotted curves above the horizontal line corresponding to the ordinate value of unity. This plot suggests that the contribution of iron to the high-temperature opacities is comparable to those of other abundant metals (like Ne and Si), while it is a less important source of opacity at low temperatures than Mg or Si. Indeed, this is also implied by the right-hand panel: the location of the giant branch appears to be more dependent on the abundances of Mg and Si than it is of Fe. However, it is clearly important to check these results by analyzing models in which the abundance of iron is varied while keeping the abundances of all of the other metals fixed. If such an investigation (which will be undertaken in the coming months) shows that iron has appreciably larger consequences for opacities and stellar models than those reported here, one would be forced to conclude that the repercussions of varying the abundances of individual metals are not additive.

Figure 10 plots the same information as in Fig. 7, except that $[\text{Fe}/\text{H}] = -2.0$ is assumed. The individual contributions of the metals to the opacities are clearly much smaller and the effects of the latter on computed evolutionary sequences (for $0.8\mathcal{M}_{\odot}$ in this case) are appreciably reduced as well. Oxygen, neon, magnesium, silicon, sulfur, and carbon all have some impact on the tracks between the ZAMS and the lower RGB, while only Mg and Si affect the location of the giant branch. At lower metal abundances, the role of the metals (other than CNO) will be of little significance, unless they have very high $[m/\text{Fe}]$ ratios. Because it affects stellar structures through the operation of the CNO-cycle, oxygen (as well as C and N, if they are sufficiently abundant) will continue to affect the turnoff and subgiant morphologies of computed tracks.

5.1.2. Consequences for Isochrones

Since most studies of stellar populations make use of isochrones, rather than evolutionary tracks, we show in Figure 11 how 12 Gyr isochrones for $[\text{Fe}/\text{H}] = -1.0$ are altered when the abundances of several metals are increased by 0.4 dex, in turn. In fact, it is unnecessary to plot the isochrones for enhanced abundances of N, Na, Ca, and Ti because they are essentially identical to that for the reference metals mixture (the solid curve). Even those for enhanced C or enhanced S are so close to the reference isochrone that it is hardly worthwhile to include them in this figure. Only the remaining four elements (O, Ne, Mg, and Si) have detectable consequences for turnoff temperatures (and, in the case of oxygen, turnoff luminosities), and

of these, only Mg and Si affect the location of the RGB. In order to show the net effect of simultaneously increasing the abundances of all of the metals that are listed in Table 1 by 0.4 dex, an isochrone for $[\text{Fe}/\text{H}] = -0.60$ (assuming the AGSC metals mix) has also been plotted. Interestingly, it appears to have close to the same turnoff luminosity as the oxygen-enhanced isochrone, which suggests that turnoff-luminosity versus age relations are not very dependent, if at all, on the abundances of the other metals (at least at low metallicities).

Indeed, further examination of these isochrones confirms this suspicion. In Figure 12, the same isochrones are replotted after applying whatever horizontal adjustments are needed in order to force all of them to have the same value of $\log T_{\text{eff}}$ at $M_{\text{bol}} \sim 5$ as the reference isochrone. (The adopted temperature offsets to achieve this are listed in the legend.) It is quite obvious that the isochrones which were computed for the AGSC mixture with separate 0.4 dex enhancements in the abundances of Ne, Mg, Si, and S have essentially identical turnoff luminosities as the reference AGSC isochrone. Only the isochrones for higher abundances of carbon (to a minor extent) and oxygen have fainter turnoffs (by $\delta M_{\text{bol}} \approx 0.02$ and 0.08 mag, respectively). As the sum of the latter is almost enough to explain the even fainter turnoff (by 0.11 mag) of the isochrone for $[\text{Fe}/\text{H}] = -0.6$, we infer that the effect of the increased iron abundance on the turnoff luminosity at a fixed age continues to be insignificant up to metallicities somewhat greater than $[\text{Fe}/\text{H}] = -1.0$.

Because O, Ne, Mg, and Si affect the difference in T_{eff} (and hence color) between the turnoff and the lower RGB *at a fixed age*, the use of such a diagnostic to determine the relative ages of star clusters having very similar $[\text{Fe}/\text{H}]$ values (e.g., VandenBerg et al. 1990) will yield reliable results only if the cluster-to-cluster differences in the abundances of these elements are small, or if the effects of such differences are taken into account. It is still a very worthwhile exercise to compare the locations of the giant branches of two or more clusters on a CMD, after their turnoffs have been superimposed, but such comparisons are clearly complicated by the fact that both age and chemical abundance differences can affect the so-called “horizontal method of determining relative ages”. Nevertheless, by considering this and additional CMD constraints (e.g., the slope of the RGB, the difference in magnitude between the HB and the turnoff, etc.), it should be possible (at least in principle) to obtain fully consistent interpretations of the observed photometric data.

As discussed above, the reduction in the turnoff luminosity of an isochrone for a fixed age that occurs when the abundances of all of the metals are enhanced by 0.4 dex appears to be due almost entirely to the increase in the oxygen abundance. (Fig. 12 considered the specific case of 12 Gyr isochrones when the adopted $[\text{Fe}/\text{H}]$ value is increased from -1.0 to -0.6 and the metals have the AGSC $[m/\text{Fe}]$ ratios.) This is not too surprising in view of the fact that, besides being the dominant source of opacity in stellar interiors (see Figs. 7–

9), oxygen constitutes most of the total C+N+O abundance that governs the rate of the CNO cycle. It was shown some time ago (VandenBerg 1992) that, at low Z , the impact of higher oxygen abundances on age-luminosity relations is due much more to the increased importance of the CNO cycle than to the concomitant increase in opacity. The updated stellar models reported here affirm and reinforce that finding by demonstrating that it also applies at higher metallicities than those considered previously.

Figure 13 plots 12 Gyr isochrones for $[\text{Fe}/\text{H}] = -1.0$ in which the effects of the heavy-element mixtures and the opacities have been decoupled. The solid and the dotted curves represent, in turn, the isochrones for the AGSC and the AGxO mixtures wherein the physics has been consistently treated. (Recall that the AGxO mixture assumes exactly the same number abundances of the metals as the AGSC mix except for a 0.4 dex increase in $[\text{O}/\text{Fe}]$.) On the other hand, isochrones derived from tracks that assume the AGSC metals mixture but the AGxO opacities, or the AGxO chemical abundances and the AGSC opacities, are shown as dot-dashed and dashed curves, respectively. In the right-hand panel, the dot-dashed isochrone has been shifted in $\log T_{\text{eff}}$ by the amount indicated in the plot, so as to match the turnoff color of the solid curve. The two isochrones obviously have nearly identical turnoff luminosities, and since they assume the same AGSC abundances, but different opacities, it follows that the increased opacity of the AGxO mixture mainly affects the predicted T_{eff} scale. On the other hand, it is apparent in the left-hand panel that the solid and the dashed isochrones, which assume different metals mixtures, but the same opacities, have quite different turnoff luminosities. Moreover, as shown in the right-hand panel, the turnoff luminosities of the dashed and dotted curves are nearly identical. Thus, it is the high oxygen *mixture* and its consequences for CNO-cycling, rather than its effects on opacities, that is almost entirely responsible for the difference in the turnoff luminosity between the solid (AGSC) and the dotted (AGxO) isochrones. Finally, the long-dashed isochrone has been plotted in the right-hand panel to show that a 13.1 Gyr isochrone for the reference AGSC mixture has the same turnoff luminosity as a 12.0 Gyr isochrone that is otherwise identical, except for the assumption of a higher oxygen abundance (specifically $[\text{O}/\text{Fe}] = 0.4$). This agrees well with previous determinations of the dependence of turnoff ages on the abundance of oxygen (e.g., VandenBerg 1992).

Figure 14 is similar to Fig. 12, except that it contains a number of isochrones for $[\text{Fe}/\text{H}] = -2.0$ instead of -1.0 . At the lower metallicity, 0.4 dex enhancements in the abundances of most of the metals are inconsequential. The only elements which do have an impact are O, Mg, and Si, and of these, only oxygen abundance variations have significant effects on turnoff-luminosity versus age relations, the difference in T_{eff} between the turnoff and the lower RGB, etc. Enhanced Mg or Si abundances mainly cause a small shift in the respective isochrone to cooler temperatures, but the effects are too small to be observationally detectable — at least

in the region of the H-R diagram that has been plotted. They do become more prominent along the upper RGB, as shown in Figure 15, which indicates that the shift in T_{eff} resulting from increased abundances of Mg or Si are about a factor of two higher near the RGB tip than near the base of the giant branch. On a color-magnitude diagram, the shift in color can be a much stronger function of luminosity, depending on the photometric indices that are used. For instance, Figure 16 shows that, when the same isochrones are plotted on the $(V - I) M_V$ diagram, the isochrones span a range in color near the tip of the RGB that is $\gtrsim 5$ times larger than at $M_V \sim 2$.⁴

Interestingly, enhanced Ca has more of an effect on the location of the RGB than all of the other metals considered here (except Mg and Si), despite its low abundance. Indeed, because isochrones for enhanced C, N, O, Ne, Na, S, or Ti barely deviate, if at all, from the isochrone for the reference mixture, they have not been plotted in Figs. 14 and 15. (Of course, the very slight shift arising from increased Ca abundances is of no significance either.) Note that the effects of varying the abundances of Mg or Si are considerably larger than those connected with a 2 Gyr change in age (the difference between the solid and long-dashed curves). Although it is well known that the giant branch is much more dependent on metallicity than on age, it has heretofore not been fully appreciated that Mg and Si are of comparable importance (at least) as Fe in determining the temperature (and color) of the RGB, and that the contribution of the other metals is insignificant.⁵ This has important ramifications for, e.g., those studies which use the differences in the colors of stars that populate the upper RGBs of very distant systems to derive ages and, in turn, the star formation histories of those objects. If there are star-to-star differences in the abundances of Mg and/or Si, the ages that are inferred from models which allow only for different $[\text{Fe}/\text{H}]$ (and perhaps $[\alpha/\text{Fe}]$) values will not be correct. In order for such studies, or any investigations that rely on a detailed understanding of giant stars, to have credible results, accurate and precise spectroscopic estimates of $[\text{Mg}/\text{Fe}]$, $[\text{Si}/\text{Fe}]$, and $[\text{Fe}/\text{H}]$ will be required,

⁴The color- T_{eff} relations that were used in creating this plot were derived by L. Casagrande (see VandenBerg et al. (2010, section 2) from synthetic spectra based on the latest MARCS model atmospheres (Gustafsson et al. 2008). The latter were computed for the AGS5 metals mixture, but with enhanced abundances of the α -elements at low metallicities; specifically, $[\alpha/\text{Fe}]$ was assumed to increase linearly from 0.0 at $[\text{Fe}/\text{H}] = 0.0$ to +0.4 at $[\text{Fe}/\text{H}] = -1.0$, and to have a constant value of +0.4 dex at lower iron abundances. Those transformations for the standard $UBV(RI)_C JHK_S$ system, together with similar relations for several *HST* ACS and WFC3 filter bandpasses will be the subject of a forthcoming paper by L. Casagrande and D. A. VandenBerg.

⁵Dotter et al. (2007) certainly recognized the importance of determining accurate abundances for Mg and Si, but they found it “hard to differentiate between the importance of low- and high-T opacities on stellar models for these two elements”.

and the effects of variations in these quantities taken into account.

5.2. Some Implications of Varying the Solar Metals Mixture

The results discussed above are based on models that assume the AGS5 solar abundances (see Table 1) with the additional $[m/\text{Fe}]$ adjustments (mainly for the α -elements) that were determined for metal-deficient stars by C04. The resultant AGSC models were compared with those obtained when several of the metals were given further abundance increases, in turn, by 0.4 dex. It is reasonable to expect that the effects of the latter will, in a differential sense, be largely independent of the base solar mixture that was initially assumed. However, how different are the AGSC isochrones from their counterparts for the GS98 solar abundances (which we have labelled “GSCX”) in an absolute sense? The answer to this question is revealed in the left-hand panel of Figure 17, which shows that, at the same values of Y , $[\text{Fe}/\text{H}]$, and age, the GSCX isochrones have fainter turnoff luminosities. This is not too surprising since there is about a 0.2 dex difference in the total C+N+O abundance between the AGS5 and GS98 solar mixtures, with the latter having the higher value of $[\text{CNO}/\text{H}]$. It is a well established result that higher CNO abundances will have the effect of reducing the turnoff luminosity at a fixed age. Confirmation of this explanation is provided by the 12 Gyr AGxO isochrone that has been included in the plot. It has a higher oxygen abundance than either the AGSC or GSCX isochrones, by 0.4 dex and ≈ 0.2 dex respectively, and it has a fainter turnoff and subgiant branch by about the expected amounts given the differences between the dashed and solid curves.

As shown in the right-hand panel, the uncertainty in the solar CNO abundances has about a 5% effect on age determinations. AGSC isochrones for $Y = 0.25$ and $[\text{Fe}/\text{H}] \lesssim -1.0$ predict ages of 12.6–12.7 Gyr at the same turnoff luminosities as 12.0 Gyr GSCX isochrones for the same chemical abundances. (Note that the indicated offsets in $\log T_{\text{eff}}$ have been applied to the AGSC loci simply to demonstrate that they do, indeed, reproduce the turnoffs and subgiant branches of the GSCX isochrones when the aforementioned age differences are assumed.) On the other hand, spectroscopic determinations of $[\text{O}/\text{H}]$ in metal-poor stars would imply higher values of $[\text{O}/\text{Fe}]$ in those stars by about 0.2 dex if the solar value of $[\text{O}/\text{H}]$ that was used to calculate $[\text{O}/\text{Fe}]$ is taken from the AGS5 determination instead of GS98. Hence, it is important to ensure that the isochrones which are used to derive ages have been computed for the correct value of $[\text{O}/\text{Fe}]$, which depends on how this quantity was derived. In fact, the models that are compared with observations should be generated for the observed absolute abundance (i.e., for the measured $\log N_i$ value, on the usual system where $\log N_{\text{H}} = 12.0$, or the $[m/\text{H}]$ value) of each of the most important elements, rather

than for such secondary abundance indicators as $[m/\text{Fe}]$.

5.3. Varying the Helium Abundance

Since the model grids reported in this investigation have been computed for three values of Y (0.25, 0.29, and 0.33) for each adopted $[\text{Fe}/\text{H}]$ value, it is worthwhile to briefly discuss the dependence of isochrones on the assumed helium abundance. As pointed out by Carney (1981) more than 30 years ago, and illustrated in the left-hand panel of Figure 18, the location on the H-R diagram of the subgiant branch of computed isochrones for a fixed age and metallicity is nearly independent of Y . Higher Y shifts both the main sequence and the giant branch to higher effective temperatures and it causes a significant reduction in the turnoff luminosity at a given age — or, equivalently, younger ages at a fixed turnoff luminosity. This effect is quantified in the right-hand panel, which shows that a 12.0 Gyr isochrone for $Y = 0.25$ has the same turnoff M_{bol} as isochrones for 11.4 Gyr, if $Y = 0.29$, or for 10.8 Gyr, if $Y = 0.33$ (assuming $[\text{Fe}/\text{H}] = -2.0$ and the AGSC metals mixture). From the information that is provided in the figure, one sees that very similar results are obtained for the $[\text{Fe}/\text{H}] = -1.0$ isochrones which have been plotted.

6. Summary

This investigation was carried out primarily to determine the impact on computed evolutionary tracks (for masses from 0.4 to $1.2M_{\odot}$) and isochrones (for ages in the range of 5–14 Gyr) of varying the abundances of each of several metals (specifically C, N, O, Ne, Na, Mg, Si, S, Ca, and Ti), in turn, at constant $[\text{Fe}/\text{H}]$ values. Indeed, extensive model grids for each of these cases have been computed for $[\text{Fe}/\text{H}]$ values ranging from -3.0 to -0.6 , in 0.2 dex increments, with $Y = 0.25, 0.29$, and 0.33 at each $[\text{Fe}/\text{H}]$ value. All of the tracks were generated using a significantly improved version of the Victoria stellar structure code, which now includes a treatment of the gravitational settling of helium and extra (turbulent) mixing very similar to the methods employed by Proffitt & Michaud (1991), as well as the latest nuclear reaction rates and conductive opacities. Fully consistent OPAL and low-temperature Rosseland mean opacities were obtained, and used, for each of the adopted heavy-element mixtures. When very similar physics is assumed, the Victoria models are found to be in excellent agreement with those based on the MESA or the University of Montreal codes. Important improvements have also been made to the Regina interpolation code, which now produces isochrones, luminosity functions, etc., from a set of evolutionary tracks very efficiently using an interactive iterative interface. Moreover, it may be used to

interpolate for arbitrary Y and $[\text{Fe}/\text{H}]$ values within the ranges for which grids of evolutionary tracks have been computed. We have verified that the interpolated grids for intermediate values of Y and $[\text{Fe}/\text{H}]$ reproduce those which are computed specifically for those abundance choices remarkably well, with respect to not only the placement of the tracks on the H-R diagram, but also the temporal derivatives of the luminosity and effective temperature along the tracks, which are important for the calculation of isochrone probability functions.

Because they are poor electron donors at low temperatures (i.e., they do not contribute significantly to low-temperature opacities), C, N, O, Ne, and S do not affect the predicted location of the giant branch. However, as they are important sources of opacity at stellar interior conditions, tracks computed for enhanced abundances of these elements are somewhat cooler and fainter. C, N, and O (especially oxygen, because of its great abundance) have bigger effects on the turnoff-luminosity versus age relations from isochrones than any other metal mainly because of their role in the CNO cycle. Higher CNO abundances imply an increased importance of the CNO cycle and thereby more centrally concentrated burning which, in turn, has the ramification that the radius of a star grows more rapidly and the turnoff is reached sooner. By contrast, the effects on isochrones due to changes in the opacity are much less important.

The remaining elements that were considered — Na, Mg, Si, Ca, and Ti — are important opacity sources at both low and high temperatures, but because of their low abundances, the effects of Na, Ca, and Ti are of no consequence (at least at low metallicities). As a result, only Mg and Si (and Fe, which is not given the same detailed analysis as the other elements) impacts the models for the RGB phase. Indeed, our study suggests that the location of the giant branch on the H-R diagram is a strong function of the abundances of Mg and Si, seemingly stronger than its dependence the iron content, which would not be too surprising given that the former are more abundant than the latter, especially in an α -element enhanced metals mixture. Mg and Si also have significant consequences for the T_{eff} scale of MS and turnoff stars: only oxygen is more important for the turnoff phase of evolution. As opacity effects are largest at the coolest temperatures, and since O, Ne, and S affect the temperatures of MS and turnoff stars but not those of giants, variations in the abundances of O, Ne, Mg, Si, and S can all affect the difference in temperature (or color) between the turnoff and the lower RGB, when measured at some luminosity above the turnoff. As a result, it is risky to use this separation as a constraint on, in particular, the relative ages of star clusters having similar iron abundances (the method first proposed by Vandenberg et al. 1990), unless the abundances of these 5 metals have been determined and the effects of cluster-to-cluster differences in them taken into account. Star-to-star variations in the abundances of Mg and Si may also be responsible for the broadening of the RGB in some GCs, and spreads in the abundances of these metals, plus O, Ne, and S, could potentially affect the width of the MS.

As long as it is clear which solar abundances (e.g., GS98, AGS5, A09) have been used in deriving the $[m/\text{Fe}]$ values from the observed m/H number-abundance ratios in metal-poor stars, and the correct $[m/\text{Fe}]$ values are assumed in the computation of the isochrones which are fitted to globular cluster CMDs, the ages so obtained should be independent of this choice. Importantly, the turnoff luminosity versus age relations from isochrones are primarily a function of the oxygen and helium abundances. Finally, we note that it is our intention to carry out a supplementary study to address a number of unanswered questions. Besides carrying out some comparisons of the observed widths of the principal photometric sequences of globular clusters with models that allow for varying abundances of several metals (notably O, Mg, and Si), the forthcoming work will isolate and examine the effects of varying the Fe abundance (keeping all other abundances fixed), and it will determine, for cases of particular interest (including Ne–Na and Mg–Al anticorrelations), the impact of varying the abundances of two elements at the same time. Such work will shed some light on whether the net effect of varying the abundances of several elements is equivalent to adding the effects due to each individual element, and it will tell us, for instance, whether the tracks and isochrones that are computed for normal Mg and Al abundances reproduce those for reduced Mg and the significantly enhanced Al abundance that would be expected (because the latter is initially much less abundant than the former) if the sum of the Mg and Al abundances is constant. (It is our intention to make the model grids that will be computed in the forthcoming study, along with a subset of those generated for the present investigation, generally available through the Canadian Astronomical Data Center. Those with a more immediate need for some of the computations reported herein are asked to contact the first author.)

We are grateful to the referee of this paper, Achim Weiss, for a number of suggestions that have led to an improved paper. We also thank Karsten Brogaard for a number of helpful suggestions on the manuscript. AD acknowledges the support of a CITA National Fellowship during the period of time when he completed most of his contribution to this project. This work has also been supported by the Natural Sciences and Engineering Research Council of Canada through Discovery Grants to DAV and GM.

REFERENCES

- Angulo, C., Arnould, M., Rayet, M., et al. 1999, *Nucl. Phys. A*, 656, 3.
- Asplund, M., Grevesse, N., & Sauval, A. J. 2005, *ASP Conf. Ser.*, 336, 25.
- Asplund, M., Grevesse, N., Sauval, A. J., & Scott, P. 2009, *ARA&A*, 47, 481.
- Bahcall, J. N., Basu, S., Pinsonneault, M., & Serenelli, A. M. 2005, *ApJ*, 618, 1049.
- Bell, R. A., & Oke, J. B. 1986, *ApJ*, 307,253.
- Bergbusch, P. A. & Vandenberg, D. A. 1992, *ApJS*, 81, 163.
- Bergbusch, P. A., & Vandenberg, D. A. 2001, *ApJ*, 556, 322.
- Bi, S. L., Li, T. D., Li, L. H., & Yang, W. M. 2011, *ApJ*, 731, L42.
- Brasseur, C. M., Stetson, P. B., Vandenberg, D. A., Casagrande, L., Bono, G., & Dall’Ora, M. 2010, *AJ*, 140, 1672.
- Burgers, J. M. 1969, *Flow Equations for Composite Gases*, (Academic Press: New York).
- Cannon, R. D., Croke, B. F. W., Bell, R. A., Hesser, J. E., & Stathakis, R. A. 1998, *MNRAS*, 298, 601.
- Carney, B. W. 1981, *IAU Colloq. No. 68, Astrophysical Parameters for Globular Clusters*, eds. A. G. D. Philip & D. S. Hayes (L. Davis Press: Schenectady, N. Y.), p. 477.
- Carretta, E., Bragaglia, A., Gratton, R. G., & Lucatello, S. 2009, *A&A*, 505, 139.
- Casagrande, L., Ramírez, I., Meléndez, J., Bessell, M., & Asplund, M. 2010, *A&A*, 512, 54.
- Cassisi, S., Potekhin, A. Y., Pietrinferni, A., Catelan, M., & Salaris, M. 2007, *ApJ*, 661, 1094.
- Cassisi, S., Salaris, M., Castelli, F., & Pietrinferni, A. 2004, *ApJ*, 616, 498.
- Cassisi, S., Salaris, M., Pietrinferni, A., Piotto, G., Milone, A. P., Bedin, L. R., & Anderson, J. 2008, *ApJ*, 672, 275.
- Cayrel, R., Depagne, E., Spite, M., et al. 2004, *A&A*, 416, 117.
- Cohen, J. G., & Meléndez, J. 2005, *AJ*, 129, 303.

- Christensen-Dalsgaard, J., Monteiro, J. J. P. F. G., Rempel, M., & Thompson, M. J. 2011, MNRAS, 414, 1158.
- Confortola, F., Bemmerer, D., Costantini, H., et al. 2007, Phys. Rev. C, 75, 065803.
- Cyburt, R. H., Fields, B. D., & Olive, K. A. 2003, Phys. Let. B, 567, 227.
- Cyburt, R. H., Fields, B. D., & Olive, K. A. 2008, JCAP, 11, 012.
- Denissenkov, P. 2012, ApJ, submitted.
- Denissenkov, P., & Vandenberg, D. A. 2003, ApJ, 593, 509.
- D’Orazi, V., Lucatello, S., Gratton, R. G., Bragaglia, A., Carretta, E., Shen, Z., & Zaggia, S. 2010, ApJ, 713, L1.
- Dotter, A., Chaboyer, B., Ferguson, J. W., Lee, H.-C., Worthey, G., Jevremović, D., & Baron, E. 2007, ApJ, 666, 403
- Eggleton, P. P. 1971, MNRAS, 151, 351.
- Ferguson, J. W., Alexander, D. R., Allard, F., Barman, T., Bodnarik, J. G., Hauschildt, P. H., Hefner-Wong, A., & Tamanai, A. 2005, ApJ, 623, 585.
- Fynbo, H. O. U., Digit, C. A., Bergmann, U. C., et al. 2005, Nature, 433, 136.
- Gratton, R. G., Bonifacio, P., Bragaglia, A., et al. 2001, A&A, 369, 87.
- Grevesse, N., & Sauval, A. J. 1998, Sp. Sci. Rev., 85, 161.
- Grundahl, F., Briley, M. M., Nissen, P. E., & Feltzing, S. 2002, A&A, 385, L14.
- Gustafsson, B., Edvardsson, B., Eriksson, K., Jørgensen, U. G., Nordlund, Å., & Plez, B. 2008, A&A, 486, 951.
- Hammer, J. W., Fey, M., Kunz, R., et al. 2005, Nucl. Phys. A, 758, 363.
- Heney, L. G., Forbes, J. E., & Gould, N. L. 1964, ApJ, 139, 306.
- Holweger, H., & Mueller, E. A. 1974, Sol. Phys., 39, 19.
- Hu, H., Glebbeek, E., Thoul, A. A., Dupret, M.-A., Stancliffe, R. J., Nelemans, G., & Aerts, C. 2010, A&A, 511, A87.
- Huebner, W. F., Merta, A. L., Magee, N. H., & Argo, M. F. 1977, Los Alamos Sci. Lab. Rep., LA-6760-M.

- Junghans, A. R., Mohrmann, E. C., Snover, K. A., et al. 2003, *Phys. Rev. C*, 68, 065803
- Junker, M., D’Alessandro, A., Zavatarelli, S., et al. 1998, *Phys. Rev. C*, 57, 2700.
- Kim, Y.-C., Demarque, P., Yi, S. K., & Alexander, D. R. 2002, *ApJS*, 143, 499.
- Korn, A. J., Grundahl, F., Richard, O., Barklem, P. S., Mashonkina, L., Collet, R., Piskunov, N., & Gustafsson, B. 2006, *Nature*, 442, 657.
- Krishna Swamy, K. S. 1966, *ApJ*, 145, 174.
- Lee, H.-c., Worthey, G., Dotter, A., Chaboyer, B., & Jevremović, D. 2009, *ApJ*, 694, 902.
- Marín-Franch, A., Aparicio, A., Piotto, G., et al. 2009, *ApJ*, 694, 1498.
- Marta, M., Formicola, A., Gyürky, Gy. et al. 2008, *Phys. Rev. C*, 78, 022802.
- Michaud, G., & Proffitt, C. R. 1993, *ASP Conf. Ser.*, 40, 246.
- Michaud, G., Richard, O., Richer, J., & Vandenberg, D. A. 2004, *ApJ*, 606, 452.
- Michaud, G., Richer, J., & Richard, O. 2010, *A&A*, 510, 104.
- Paquette, C., Pelletier, C., Fontaine, G., & Michaud, G. 1986, *ApJS*, 61, 177.
- Paxton, B., Bildsten, L., Dotter, A., Herwig, F., Lesaffre, P., & Timmes, F. 2011, *ApJS*, 192, 3.
- Pietrinferni, A., Cassisi, S., Salaris, M., & Castelli, F. 2006, *ApJ*, 642, 797.
- Pietrinferni, A., Cassisi, S., Salaris, M., Percival, S., & Ferguson, J. W. 2009, *ApJ*, 697, 275.
- Pinsonneault, M. H., & Delahaye, F. 2009, *ApJ*, 704, 1174.
- Proffitt, C. R., & Michaud, G. 1991, *ApJ*, 371, 584.
- Proffitt, C. R., & Vandenberg, D. A. 1991, *ApJS*, 77, 473.
- Ramírez, I., & Cohen, J. 2002, *AJ*, 123, 3277.
- Richard, O., Michaud, G., & Richer, J. 2001, *ApJ*, 558, 377.
- Richard, O., Michaud, G., Richer, J., Turcotte, S., Turck-Chièze, S., & Vandenberg, D. A. 2002, *ApJ*, 568, 979.
- Richer, J., Michaud, G., & Turcotte, S. 2000, *ApJ*, 529, 338.

- Rood, R. T., & Crocker, D. A. 1985, in *Production and Distribution of C, N, O Elements*, eds. I. J. Danziger, F. Matteucci, & K. Kj ar (Garching: ESO), 61.
- Salaris, M., Chieffi, A., & Straniero, O. 1993, *ApJ*, 414, 580.
- Salaris, M., Weiss, A., Ferguson, J. W., & Fusilier, D. J. 2006, *ApJ*, 645, 1131.
- Sbordone, L., Salaris, W., Weiss, A., & Cassisi, S. 2011, *A&A*, 534, A9.
- Serenelli, A. M., Basu, S., Ferguson, J. W., & Asplund, M. 2009, *ApJ*, 705, L123.
- Shetrone, M., Martell, S. L., Wilkerson, R., Adams, J., Siegel, M. H., Smith, G. H., & Bond, H. E. 2010, *AJ*, 140, 1119.
- Spite, F., & Spite, M. 1982, *A&A* 115, 357.
- Thoul, A. A., Bahcall, J. N., & Loeb, A. 1994, *ApJ*, 421, 828.
- Turcotte, S., Richer, J., Michaud, G., Iglesias, C. A., & Rogers, F. J. 1998, *ApJ*, 504, 539.
- VandenBerg, D. A. 1985, in *Production and Distribution of C, N, O Elements*, eds. I. J. Danziger, F. Matteucci, & K. Kj ar (Garching: ESO), 73.
- VandenBerg, D. A. 1992, *ApJ*, 391, 685.
- VandenBerg, D. A., & Bell, R. A. 2001, *New Astron. Rev.*, 45, 577.
- VandenBerg, D. A., Bergbusch, P. A., & Dowler, P. D. 2006, *ApJS*, 162, 375.
- VandenBerg, D. A., Bolte, M., & Stetson, P. B. 1990, *AJ*, 100, 445.
- VandenBerg, D. A., Casagrande, L., & Stetson, P. B. 2010, *AJ*, 140, 1020.
- VandenBerg, D. A., Edvardsson, B., Eriksson, K., & Gustafsson, B. 2008, *ApJ*, 675, 746.
- VandenBerg, D. A., & Poll, H. E., 1989, *AJ*, 98, 1451.
- VandenBerg, D. A., & Stetson, P. B. 1991, *AJ*, 102, 1043.
- VandenBerg, D. A., Swenson, F. J., Rogers, F. J., Iglesias, C. A., & Alexander, D. R. 2000, *ApJ*, 532, 430.
- Yong, D., Grundahl, F., Nissen, P. E., Jensen, H. R., & Lambert, D. L. 2005, *A&A*, 438, 875.

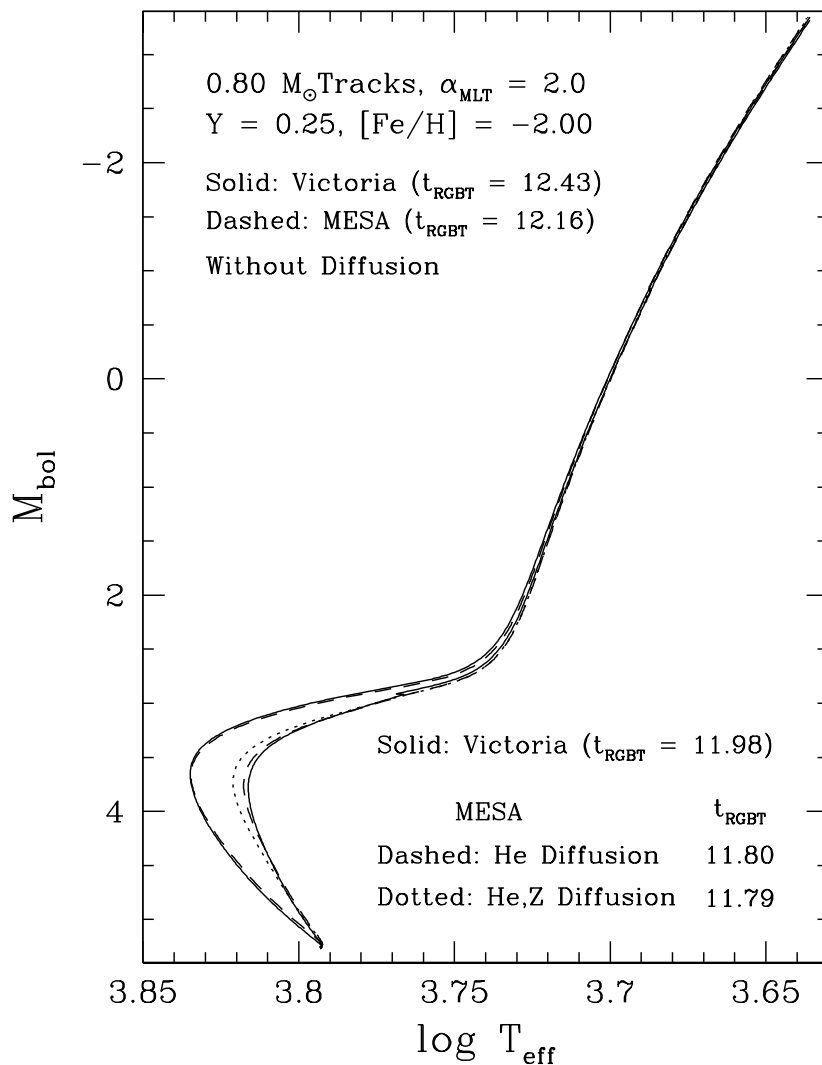


Fig. 1.— Comparison of evolutionary tracks computed using the Victoria and the MESA codes for the indicated mass and initial chemical abundances if the gravitational settling of helium is treated (the coolest sequences) and if diffusive processes are ignored (the hottest tracks). Predicted ages at the RGB tip are given in Gyr. Extra (turbulent) mixing is not considered.

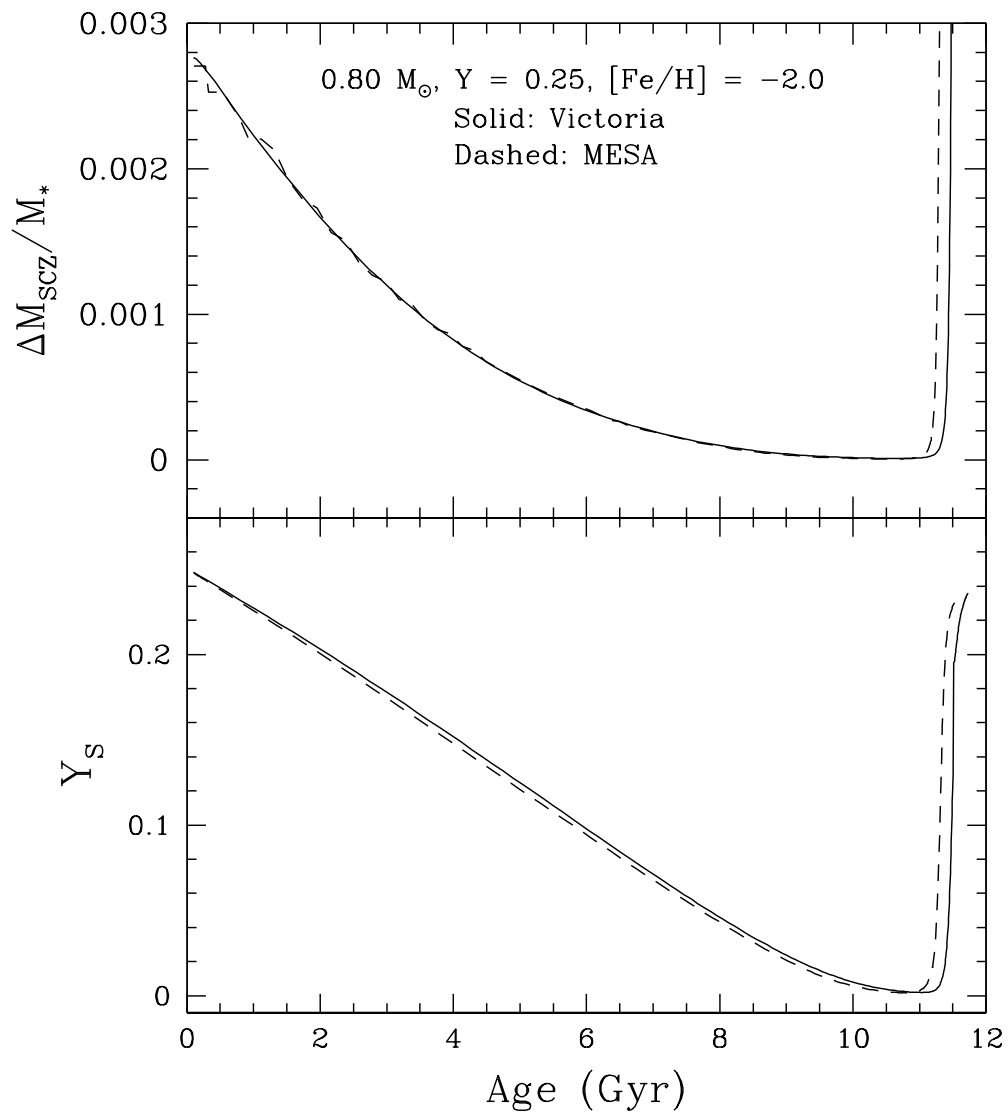


Fig. 2.— The predicted variations with age of the fractional envelope mass in the surface convection zone (upper panel) and the surface mass-fraction abundance of helium for the ZAMS to lower RGB portions of the diffusive tracks shown in the previous figure. Extra mixing due to turbulence is not taken into account.

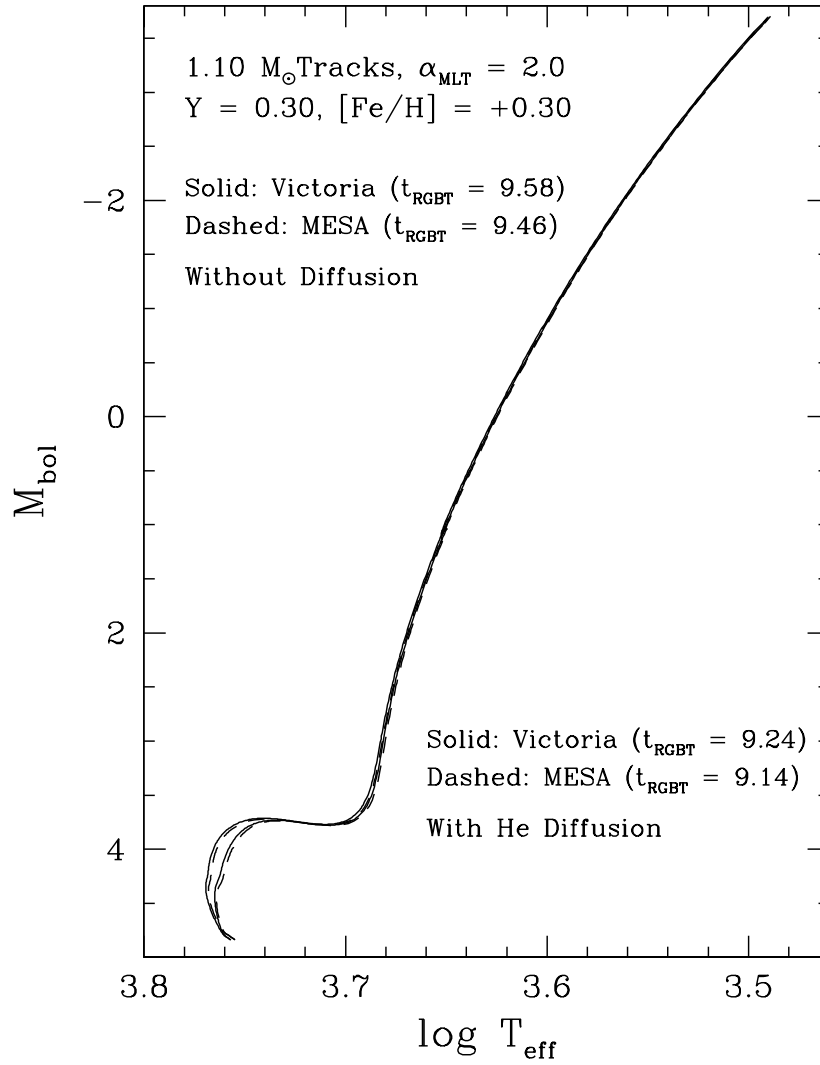


Fig. 3.— As in Fig. 1, except that tracks have been computed for a higher mass and higher initial values of Y and $[\text{Fe}/\text{H}]$, as indicated. Extra (turbulent) mixing is not treated.

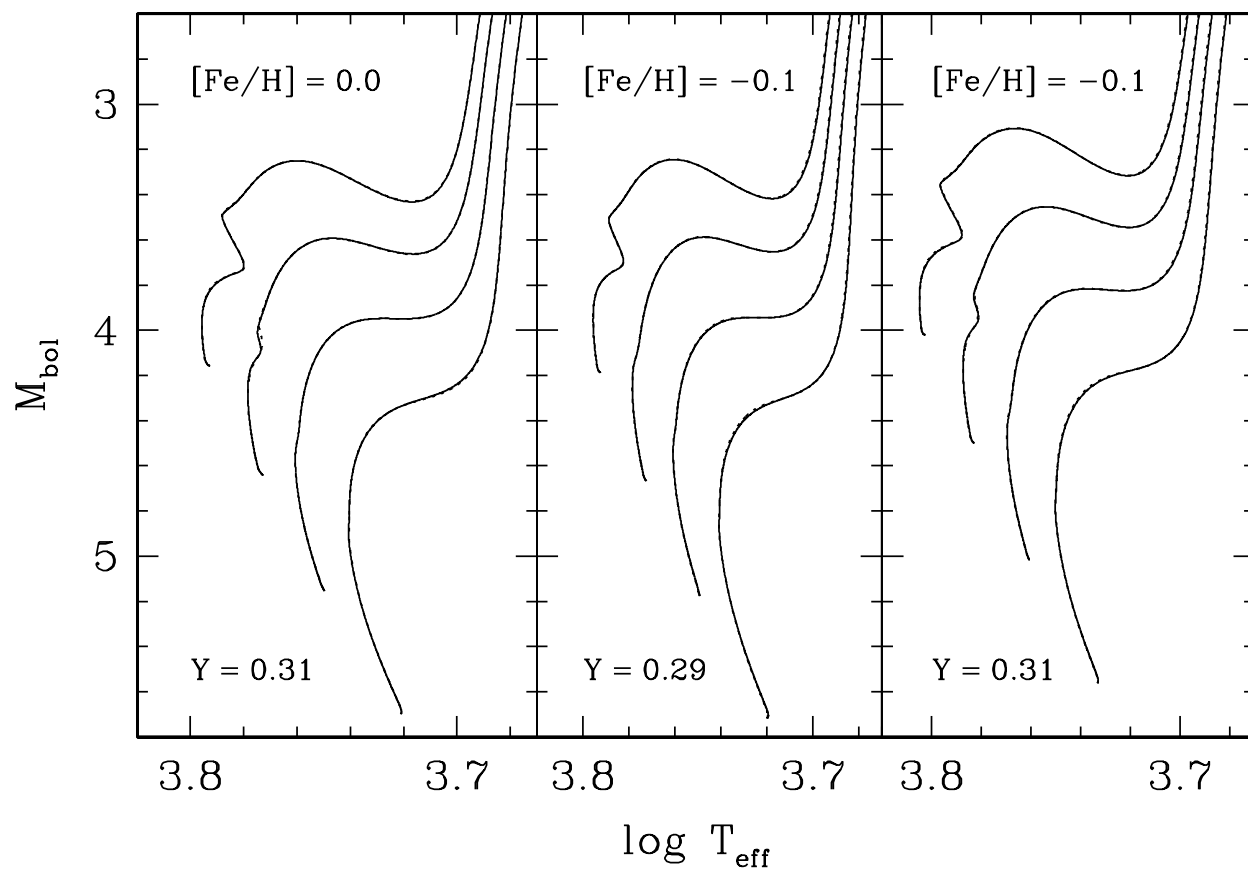


Fig. 4.— $1.2, 1.1, 1.0,$ and $0.9M_{\odot}$ evolutionary tracks from a special test grid computed directly using the Victoria code are plotted as *solid* lines. Tracks for the same abundance parameters interpolated from the canonical grids are superimposed as *dotted* lines. The panels, in the direction from left to right, show examples of interpolations in Y only, in $[\text{Fe}/\text{H}]$ only, and in both Y and $[\text{Fe}/\text{H}]$. In general, the agreement is astonishingly good, as it is almost impossible to distinguish between the two sets of tracks.

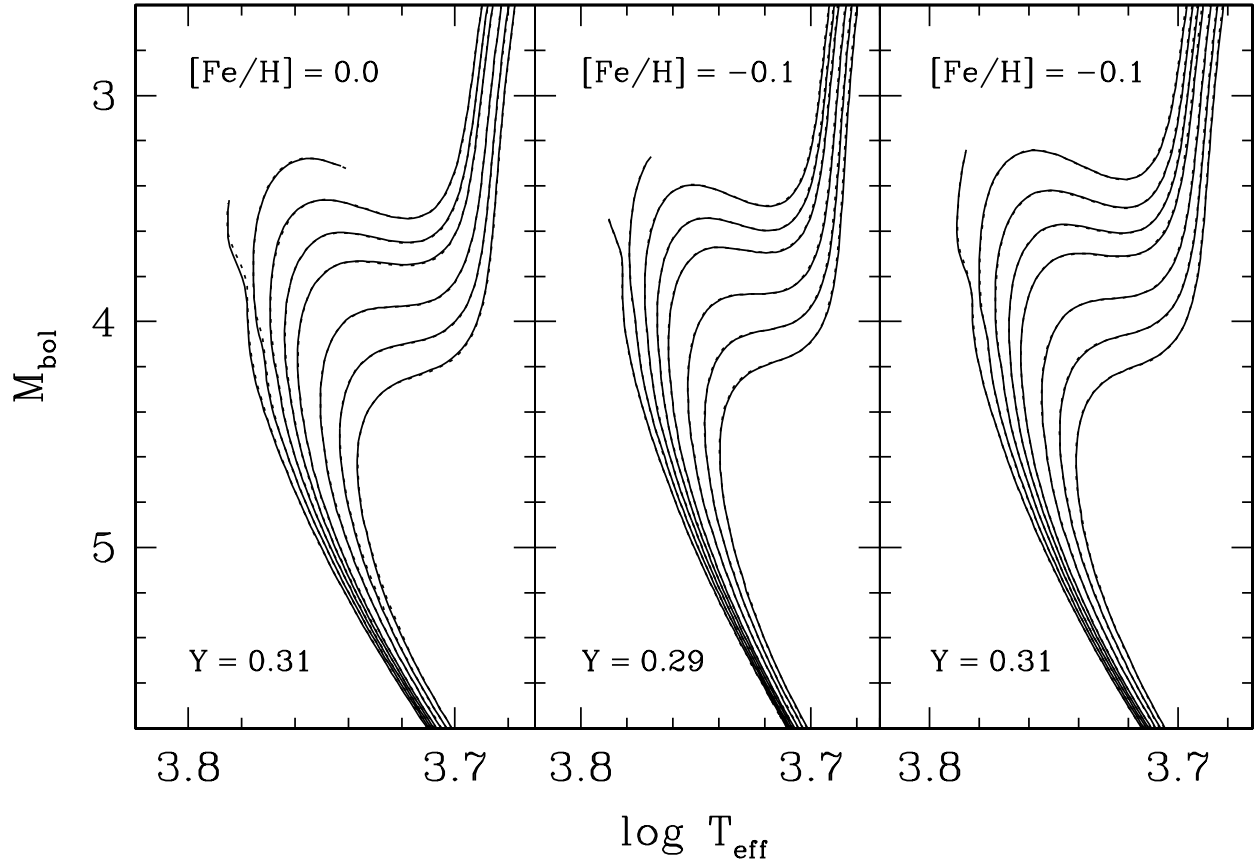


Fig. 5.— 4, 5, 6, 7, 8, 10, 12, and 14 Gyr isochrones interpolated directly from the specially computed test grid are plotted as *solid* lines. Isochrones interpolated from the interpolated tracks are superimposed as *dotted* lines. The experiments shown in each panel correspond to those illustrated in the previous figure.

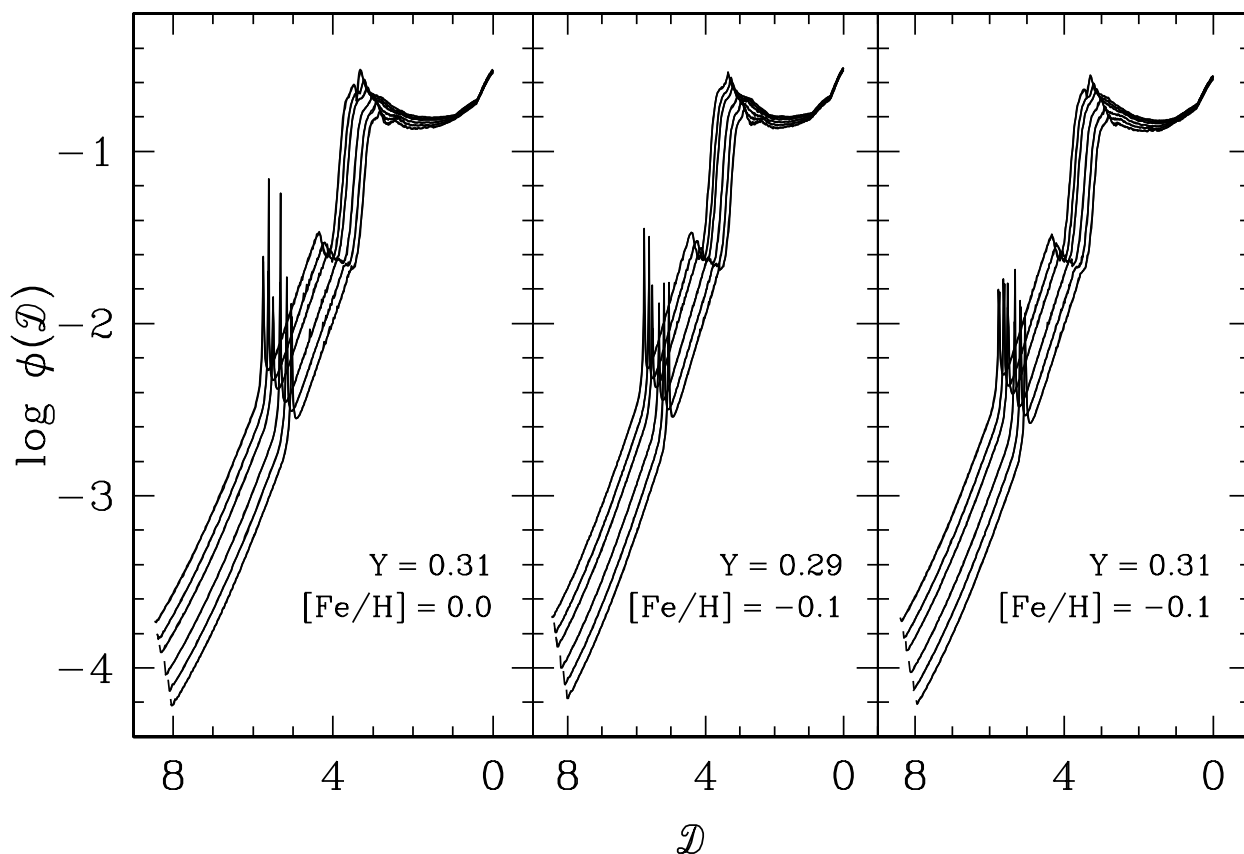


Fig. 6.— Differential isochrone population functions for 4, 5, 6, 7, 8, 10, 12, and 14 Gyr interpolated directly from the special test grid of tracks are plotted as *solid* lines, while those interpolated from the interpolated grids are superimposed as *dotted* lines. The differences between the two sets of DIPFs are too small to be seen at the scale of these plots. The experiments shown in each panel correspond to those illustrated in Fig. 4. Note that the zero-point of the abscissa coincides with the position on the H-R diagram of the lowest-mass model that has been considered, which is for $0.4M_{\odot}$.

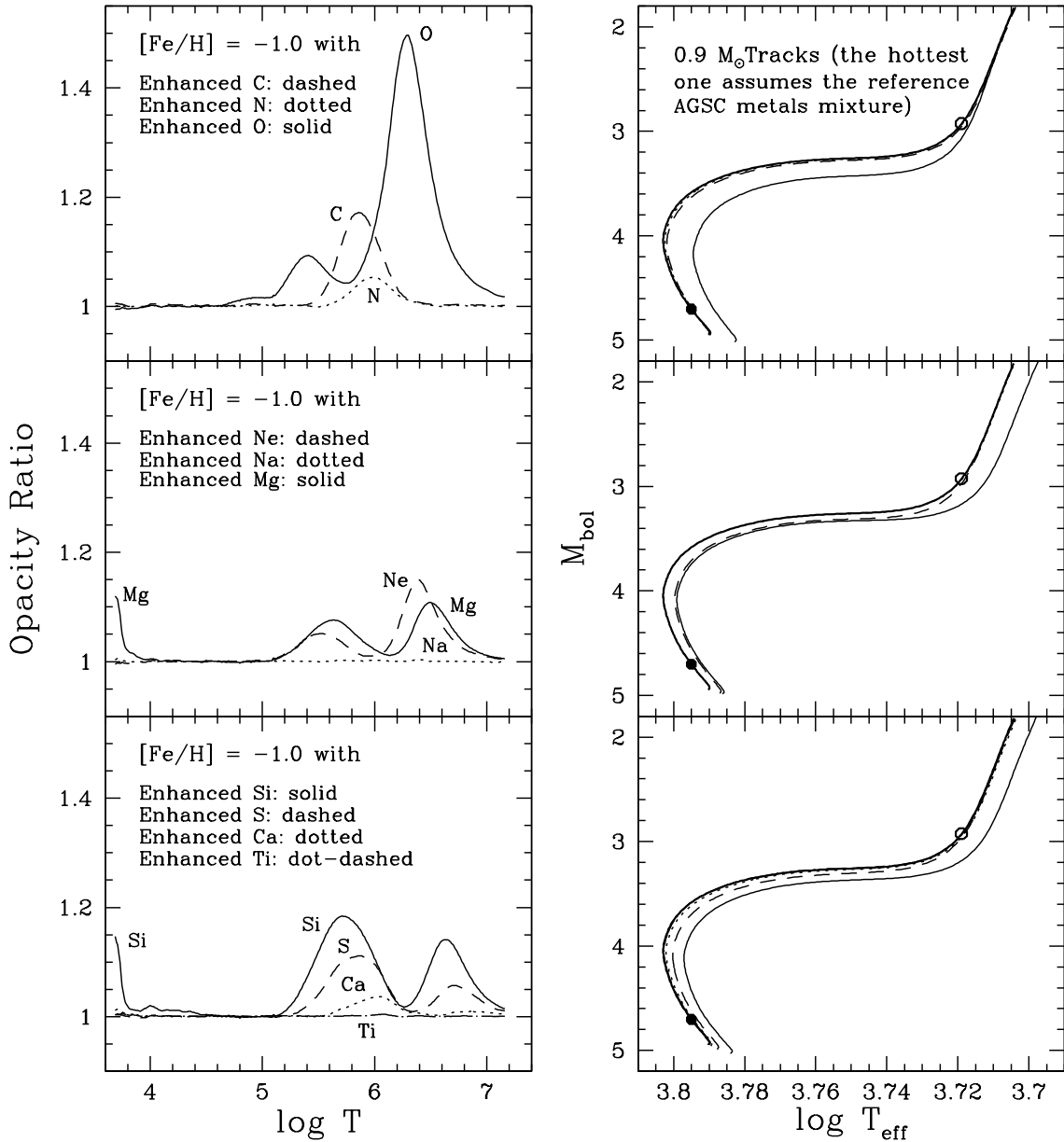


Fig. 7.— The left-hand panels plot ratios of the opacity for each of the mixtures with an enhanced abundance of a single metal, as indicated, to that for the reference AGSC mixture, assuming $[\text{Fe}/\text{H}] = -1.0$. The temperatures, densities, and hydrogen mass-fraction abundances that were assumed in the determination of the opacities (by interpolations in tables) correspond to the surface-to-center variations in the model that has been plotted as a filled circle in the right-hand panels. (The structural properties of the lower RGB model represented by the open circle are used to generate the opacity data that are plotted in the next figure.) The definitions of the line types that are given in the left-hand panels also apply to the adjacent H-R diagrams, which show the impact of the same abundance enhancements on computed tracks between the ZAMS and the lower RGB.

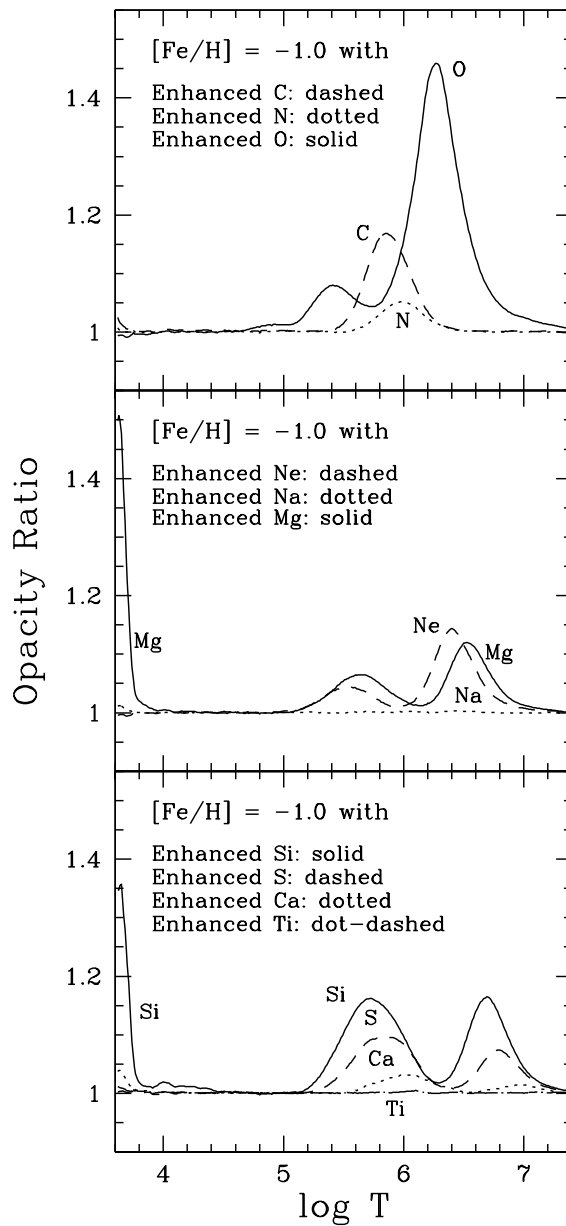


Fig. 8.— As in the left-hand panels of the previous figure, except that the opacity ratios have been computed for the values of ρ , X_{H} , and T from the surface to the center of the lower RGB model that has been plotted as an open circle in the right-hand panels of that figure.

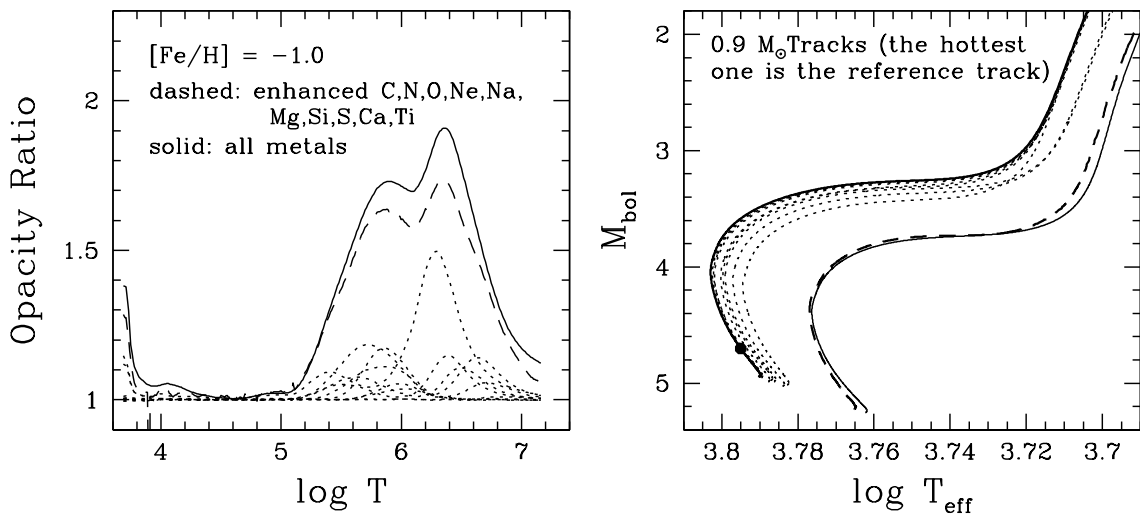


Fig. 9.— As in Fig. 7, except that all of the loci are plotted in the same panels as *dotted* curves. The sums of the effects of increasing the abundance of each metal on the opacity and on evolutionary tracks are shown as *dashed* curves. The differences between the latter and the thin solid curves are (tentatively; see the text) attributed to a 0.4 dex increase in the abundance of iron (primarily), when the abundances of the 10 metals considered here are held constant. Note that the predicted RGBs for the tracks with enhanced Mg or enhanced Si overlap one another. The elements that have the biggest effects in the vicinity of the turnoff are O and Si, followed by Mg and Ne.

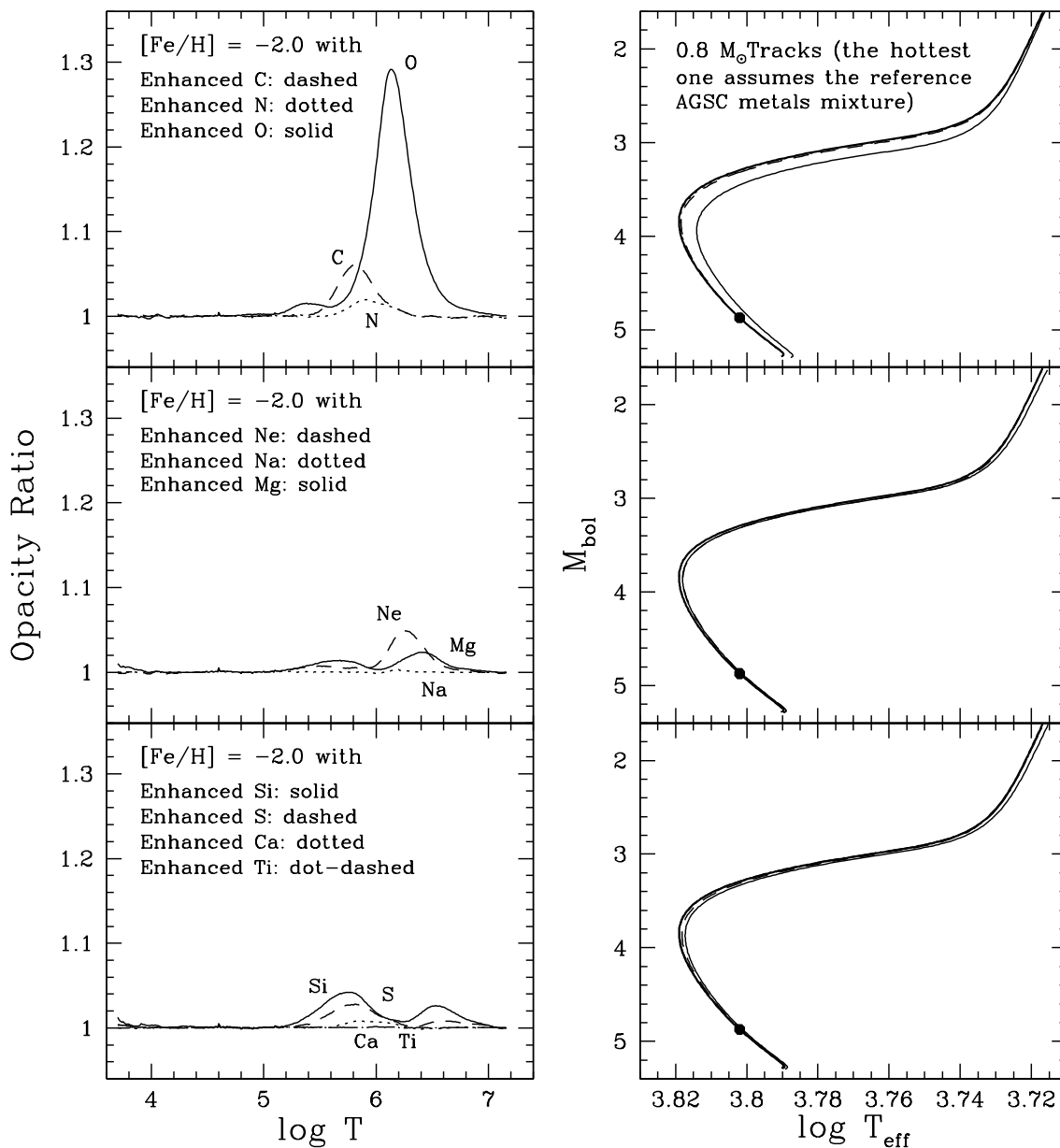


Fig. 10.— As in Fig. 7, except for $[\text{Fe}/\text{H}] = -2.0$. Note that the range of the ordinate has been reduced, and that the evolutionary tracks for Ne and Mg overlay one another from the ZAMS until just before the base of the RGB, at which point they separate.

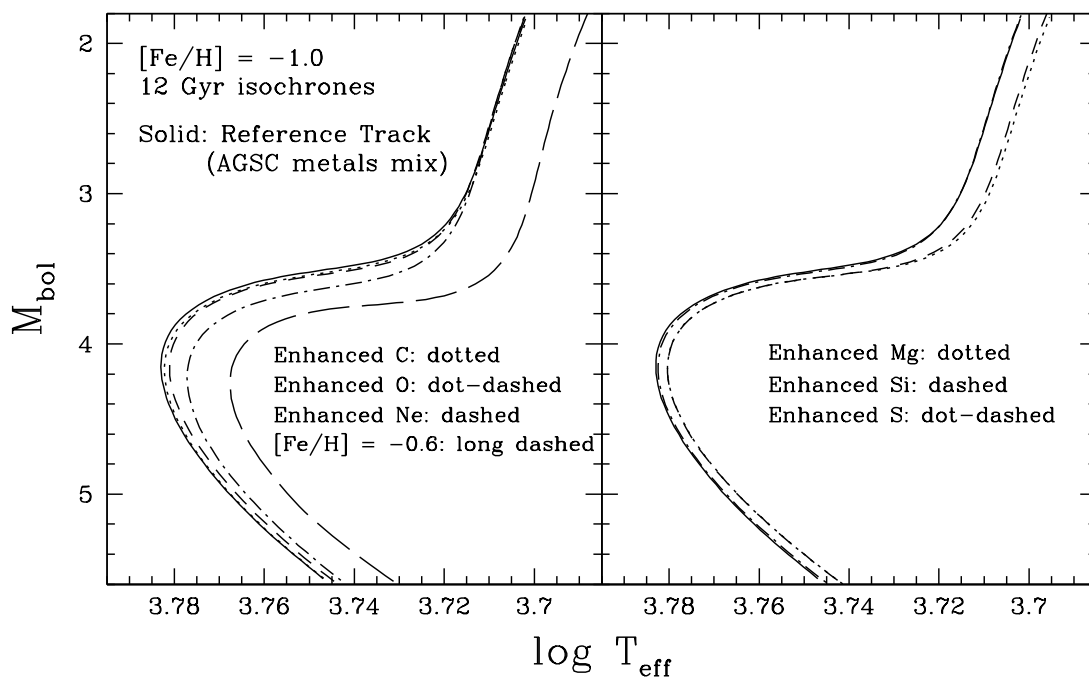


Fig. 11.— Comparison of isochrones for $Y = 0.25$ and $[\text{Fe}/\text{H}] = -1.0$ with, and without, 0.4 dex enhancements in the abundances of C, O, Ne, Mg, Si, and S (in turn). An isochrone for the same AGSC metals mixture as the *solid* curve, but for $[\text{Fe}/\text{H}] = -0.6$, has also been plotted to show the impact, relative to the reference isochrone, of increasing the abundances of all of the metals by 0.4 dex.

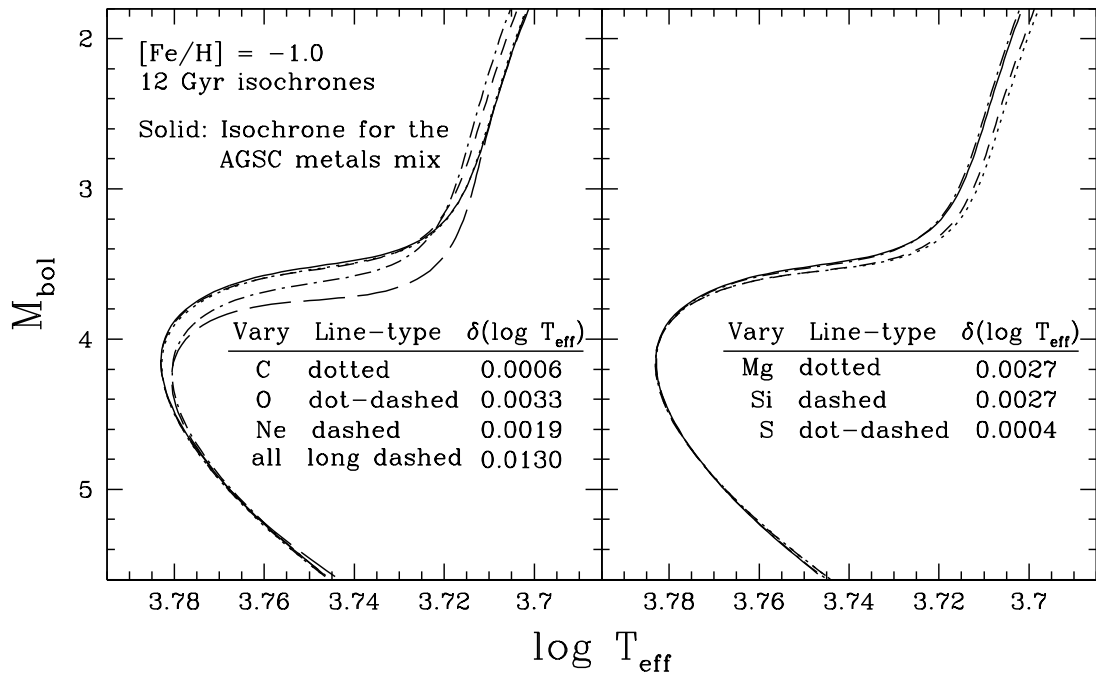


Fig. 12.— As in the previous figure, except that all of the isochrones have been shifted horizontally so that they coincide with the reference isochrone (the *solid* curve) at $M_{\text{bol}} = 5.0$. The offsets in $\log T_{\text{eff}}$ that have been applied are specified in the legend.

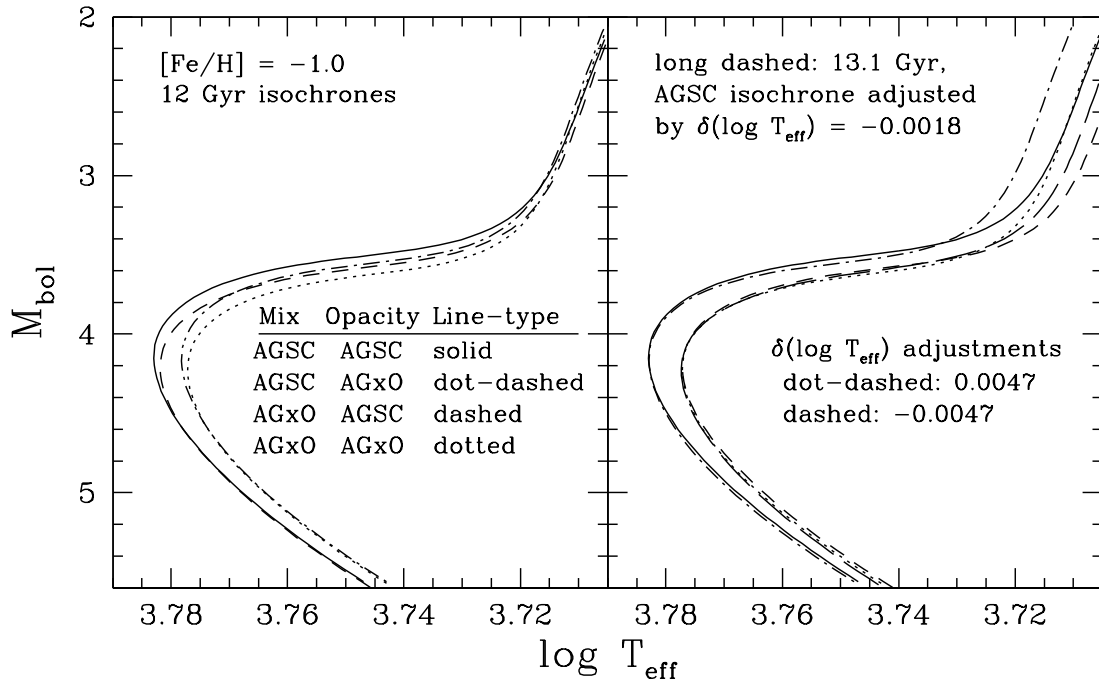


Fig. 13.— The left-hand panel compares isochrones for the AGSC and AGxO cases (*solid* and *dotted* curves, respectively), with those in which the opacities that were used to generate the models were not consistent with the assumed heavy-element mixtures. To be specific, the *dot-dashed* isochrone assumes the AGSC metals mix and the AGxO opacities, while the *dashed* isochrone assumes the AGxO mixture and the AGSC opacities. The right-hand panel shows that, when the *dot-dashed* and *dashed* isochrones are shifted in temperature by the amounts indicated, they have very close to the same turnoff luminosities as the *solid* and *dotted* isochrones, respectively.

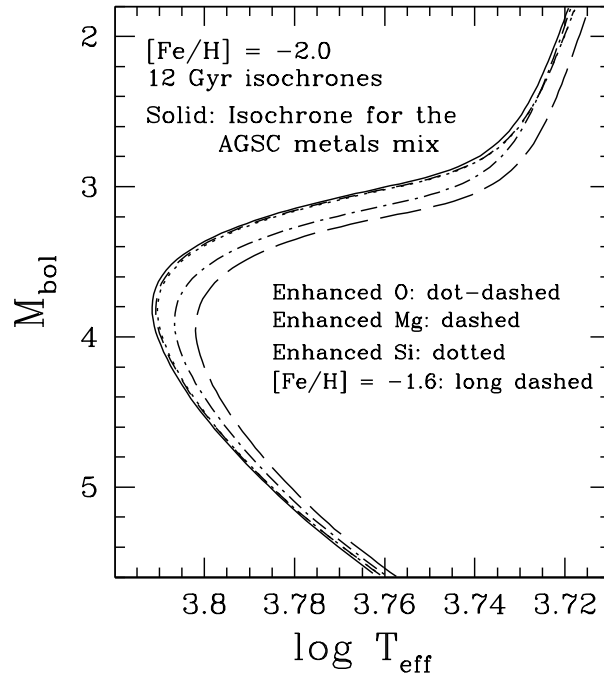


Fig. 14.— Similar to Fig. 12, except for $[\text{Fe}/\text{H}] = -2.0$. Isochrones that allow for 0.4 dex enhancements in the abundances of single metals are identical with the reference (AGSC) isochrone (the *solid* curve), except in the case of O, Mg, and Si. An isochrone for $[\text{Fe}/\text{H}] = -1.6$ has also been plotted to show the effects of simultaneously increasing the abundances of all of the metals by 0.4 dex.

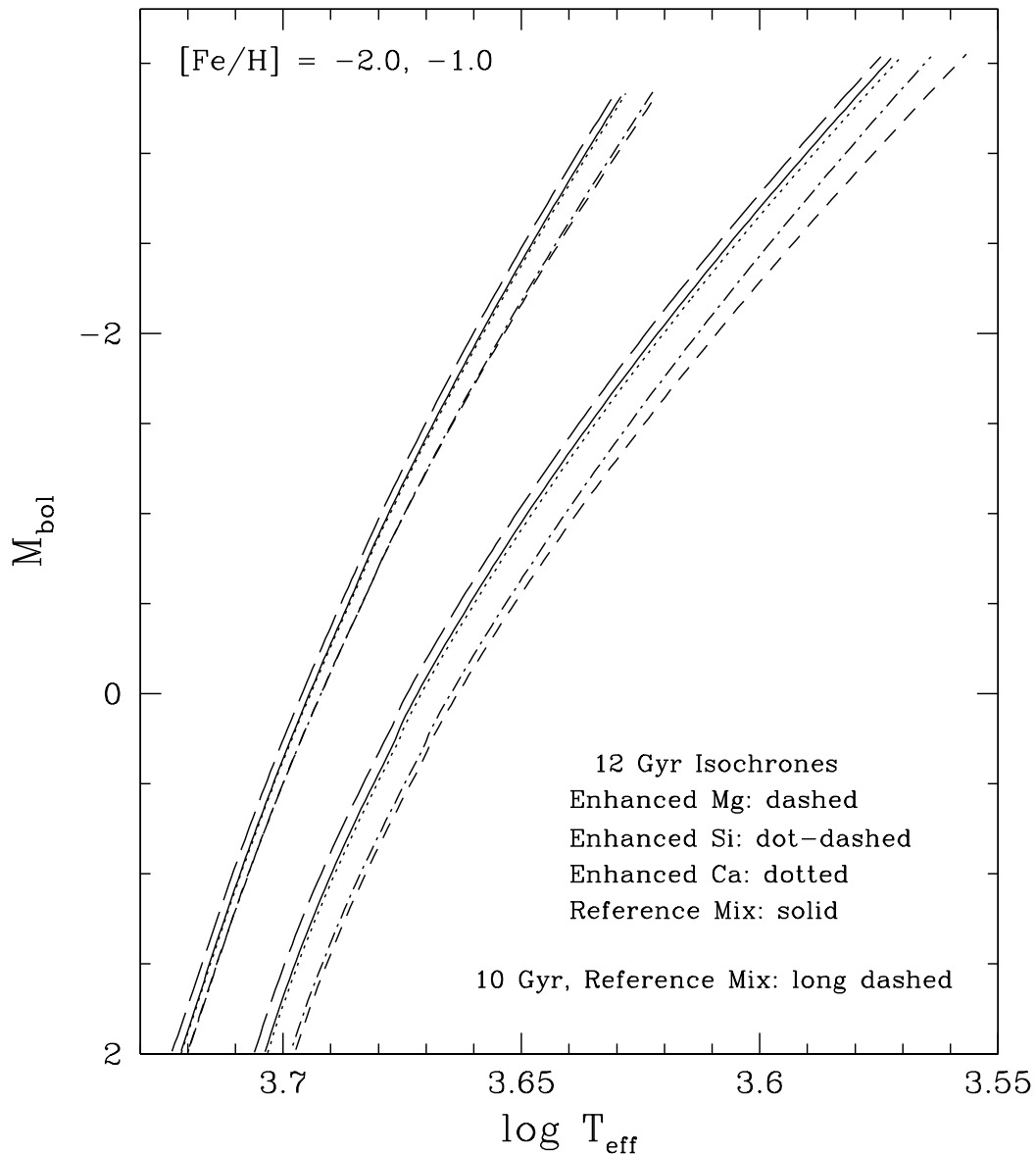


Fig. 15.— Plot of the giant-branch segments of 12 Gyr isochrones for $[Fe/H] = -2.0$ (the hotter RGBs) and -1.0 when enhanced abundances of Mg, Si, and Ca are assumed, in turn (as indicated). The *solid* and the *dashed* loci represent 12 and 10 Gyr isochrones, respectively, for the reference AGSC metals mixture.

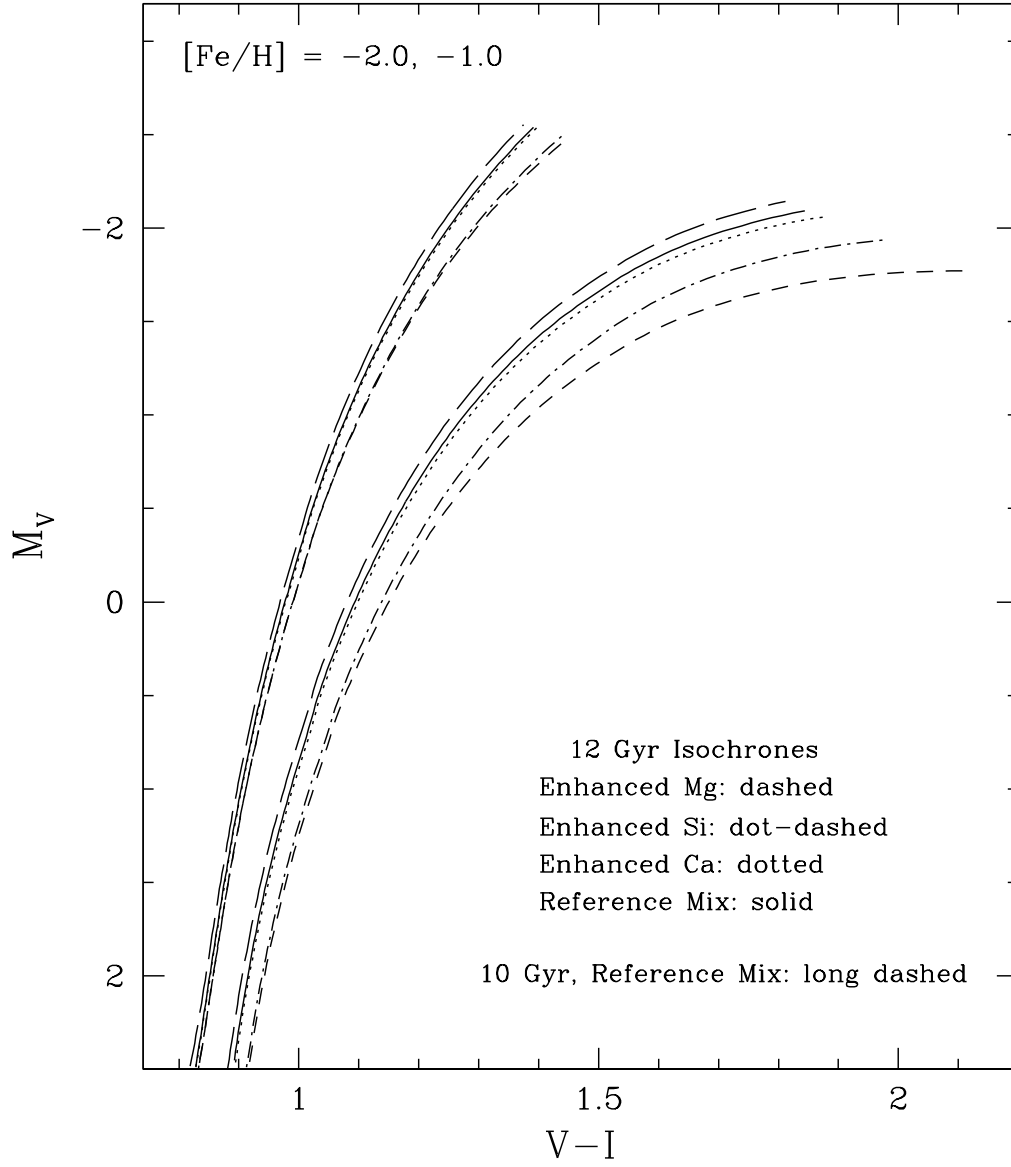


Fig. 16.— As in the previous figure, except that the RGBs of the same isochrones have been plotted on the $(V - I) M_V$ diagram.

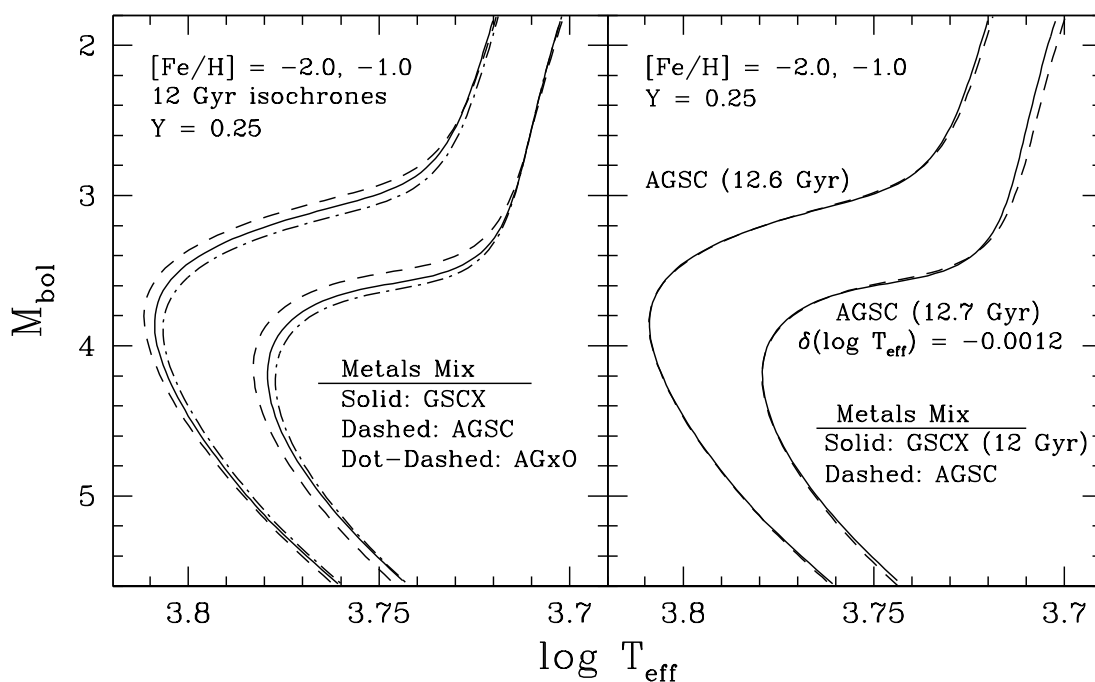


Fig. 17.— The left-hand panel compares AGSC, GSCX, and AGxO isochrones for an age of 12 Gyr and the indicated Y and $[\text{Fe}/\text{H}]$ values. The right-hand panel shows that, in order to reproduce the turnoff luminosities of 12 Gyr GSCX isochrones, the AGSC isochrones must have higher ages by $\approx 5\%$. The predicted temperatures along the latter have been adjusted by the indicated amounts to show that they provide an excellent match to the GSCX isochrones in the vicinity of the turnoff.

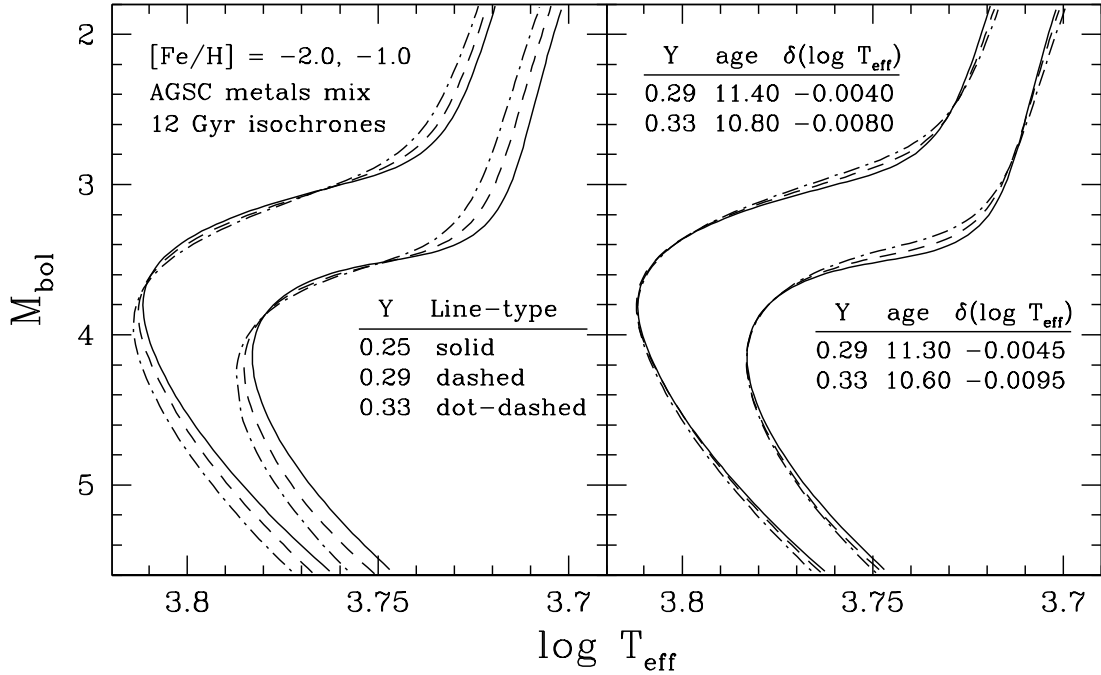


Fig. 18.— The left-hand panel illustrates the effect of varying Y on 12 Gyr isochrones for $[\text{Fe}/\text{H}] = -2.0$ and -1.0 (assuming the AGSC metals mix). The right-hand panel compares 12 Gyr isochrones for $Y = 0.25$ with those for $Y = 0.29$ and 0.33 , assuming those ages for the latter such that all three of the isochrones for a given $[\text{Fe}/\text{H}]$ value have the same turnoff luminosities. The higher Y isochrones were adjusted in $\log T_{\text{eff}}$ by the indicated amounts simply to show that they provide a close match to the turnoff of the *solid* curve.

Table 1. Adopted Heavy-Element Mixtures

Element	$\log N^a$			$\Delta \log N$	
	A09 ^b	GS98 ^c	AGS5 ^d	C04 ^e	extra ^f
C	8.43	8.52	8.39	0.00	0.40 (AGxC)
N	7.83	7.92	7.78	0.00	0.40 (AGxN)
O	8.69	8.83	8.66	0.50	0.40 (AGxO)
Ne	7.93	8.08	7.84	0.30	0.40 (AGNe)
Na	6.24	6.33	6.17	0.00	0.40 (AGNa)
Mg	7.60	7.58	7.53	0.30	0.40 (AGMg)
Al	6.45	6.47	6.37	0.00	
Si	7.51	7.55	7.51	0.40	0.40 (AGSi)
P	5.41	5.45	5.36	0.00	
S	7.12	7.33	7.14	0.30	0.40 (AGxS)
Cl	5.50	5.50	5.50	0.00	
Ar	6.40	6.40	6.18	0.25	
K	5.03	5.12	5.08	0.00	
Ca	6.34	6.36	6.31	0.30	0.40 (AGCa)
Ti	4.95	5.02	4.90	0.25	0.40 (AGTi)
Cr	5.64	5.67	5.64	−0.30	
Mn	5.43	5.39	5.39	−0.40	
Fe	7.50	7.50	7.45	0.00	
Ni	6.22	6.25	6.23	0.00	

^aOn the scale in which $\log N(\text{H}) = 12.0$

^bA09 = Asplund et al. (2009)

^cGS98 = Grevesse & Sauval (1998)

^dAGS5 = Asplund, Grevesse, & Sauval (2005)

^eC04 = Cayrel et al. (2004)

^fSeparate model grids, with the name identification given in the parentheses, were generated for the “AGS5 + C04 + extra” metal abundances, scaled to many $[\text{Fe}/\text{H}]$ values